The People's Democratic Republic of Algeria
Ministry of Higher Education and Scientific Research

Amar Telidji University - Laghouat

Faculty of Sciences

Doctoral Thesis

Specialty: Material Physics

Publicly presented on

11/06/2022

by:

Mohamed Abdelilah FADLA

Title

Theoretical calculation of physical properties for some new potential perovskites for solar energy conversion.

Thesis committee:

Ibn khaldoun LEFKAIER	**President**	Pr, Amar Telidji University, Laghouat
Bachir BENTRIA	**Supervisor**	Pr, Amar Telidji University, Laghouat
Nadjib BAADJI	**Examiner**	Pr, University of M'sila
Youcef BOUHADDA	**Examiner**	Pr, URAER, Ghardaïa
Ahmed GUEDDOUH	**Examiner**	Dr, Amar Telidji University, Laghouat

Acknowledgments

First, I would like to express my sincere gratitude to all LPM members. All the work presented in this thesis was entirely carried out in the "Laboratoire de Physique des Matériaux" (LPM), University of Amar Telidji, Laghouat. With special thanks to Pr. Ibn-Khaldoun Lefkaier laboratory director, all Groups Leaders, and all my professors in the Department of Materials Science.

Further, my sincere thanks to my supervisor Pr. Bachir Bentria for the thoughtful comments, valuable recommendations and suggestions, his consistent support and guidance in all stages of this work, despite extremely busy schedule. He spent much time to improve the quality of this thesis. Great thanks for your confidence and the freedom you gave me to do my PhD. Without you this work would not have been possible.

I also would like to thank Mr. Tahar Dahame my co-supervisor in my master's degree, for his unconditional support and the fruitful discussions.

I am profoundly grateful to Mr. LEFKAIER Ibn khaldoun, to have accepted to chair the jury of this thesis. My sincere thanks to jury member Mr. BAADJI Nadjib, Mr BOUHADDA Youcef and Mr. GUEDDOUH Ahmed for agreeing to read the manuscript.

I am profoundly grateful to Mr. Guido Roma Université Paris-Saclay, CEA, Service de Recherches de Métallurgie Physique. Who helped me learn a lot about inorganic perovskite material, especially my work on point defect.

I sincerely thank Mr. Christoph Freysoldt, Defect Chemistry and Spectroscopy group Leader, Department Computational Materials Design Max-Planck-Institut für Eisenforschung,

for all his thoughtful comments that help me to gain a better understanding of defects modeling, on both technical and theoretical sides.

I would like to thank my colleagues “brothers” at the research laboratories complex Mr. Fares Faid, Mr. Ali Benghia, Mr. Adel Allal, Mr. Fakhereddine Khemloul, and Mr. Youcef Daoudi.

My sincere thanks go to Mr. El Tayeb Bentria and Mr. Brahim Marfoua who left, but always are giving me their supports.

Abstract

Organometallic perovskite solar cells have attracted great attention in the last years. They exhibit very low production cost, due to their simple preparation method, coupled to high power conversion efficiencies (up to 26% for Formamidinium Lead iodide perovskite $FAPbI_3$). This is achieved after just few years following their discovery. However, organometallic perovskite are very sensitive to moisture, oxygen and light due to the presence of organic cations. The smaller cesium cation has been used to replace organic cations to resolve the instability issues of organometallic perovskite. In this thesis, first principle computation method is used to understand perovskite's high power conversion efficiency. The structural stability, electronic and optical properties of $CsPbI_3$ polymorphs are investigated as well as some carrier transport properties. The lower symmetry orthorhombic Pnam black phase is more energetically favourable compared to tetragonal phase and the high symmetric cubic phase. Lead as well as iodide atoms play significant role in the high optical absorption (more $10^5 Cm^{-1}$). Mixed halide perovskite $CsPb(I_{1-x}Br_x)_3$ at low symmetry black phase (Pnam) are investigated to increase material stability and adjust the optoelectronic properties. The iodine bromine partial substitution significantly enhances material stability. The carrier mobility are computed through deformation potential theory, and both $CsPbI_3$ and $CsPbBr_3$ compounds show very low effective mass. Band alignment approach is used to find suitable electron and hole transport materials. By means of super cell approach as well as FNV-KO scheme, the defect tolerance of cesium lead halide perovskite is discussed by studying all possible intrinsic point defects. Several defects create shallow levels, while the

intrinsic defects that may create deep levels have high formation energies especially under Iodine and Bromine poor conditions.

ملخص

خلايا البيروفسكايت الشمسية تم التركيز عليها بشدة خلال السنوات الأخيرة. لأنها تحضر بطريقة بسيطة مما سيجعلها من أرخص التكنولوجيات الكهروضوئية. إضافة الى كفاءتها العالية في تحويل الطاقة بنسبة (26) خلال سنوات قليلة من اكتشافها. تعتبر خلايا البيروفسكايت الهجينة غير مستقرة وحساسة جدا للضوء، الرطوبة او الاكسجين نظرا لوجود الجزيئات العضوية FA و MA
كاتيونات السيزيوم ذات القطر الايوني الأصغر تم استعمالها لحل هذه المشكلة. خلال هذا العمل تم استخدام حساب المبادئ الأساسية لفهم الكفاءة العالية لخلايا البيروفسكايت للمركب $CsPbI_3$ والتركيز على الهياكل متعددة الاشكال عبر دراسة استقرارها وخصائصها البنيوية إضافة الى العديد من الخصائص الالكترونية والضوئية وبعض خصائص النقل لكل من الإلكترونات والثقوب. تبين ان المركب ذو البنية المعينة القائمة والتي تعبر الأقل تناظرا بين الهياكل المدروسة هي الأكثر استقرارا. من خلال دراسة كثافة الحالة وجد ان ذرات الرصاص وبصفة اقل ذرات اليود مسؤولان عن معامل الامتصاص المرتفع لهذه الخلايا (أكثر من 10^5).
بعد ذلك تم استخدام البروم لاستبدال اليود جزئيا وكليا لزيادة استقرار الخلايا من جهة والتحكم في فجوة الطاقة ومختلف الخصائص. إضافة الى استخدام نظرية التشوه الكموني المرن لدراسة الحركية. وبالتحديد الدقيق للمستويات الطاقة تم اقتراح مواد ملائمة لنقل الالكترونات والثقوب في الخلايا الشمسية غرض الحصول على اعلى كفاءة ممكنة لهذه الخلايا.

بعد ذلك تم دراسة العيوب وتفسير السماحة العالية لهذه المركبات. وجد ان اغلب العيوب تنشئ مستويات سطحية والعيوب التي من الممكن ان تشكل مستويات عميقة يمكن التحكم في طاقة تشكيلها عبر تغيير ظروف التفاعل بالذهاب نحو وسط اكثر فقرا للبروم او اليود

List of abbreviations

Theory

DFT	Density Functional Theory
PW	Plane wave
PP	Pseudo potential
PAW	Projected augmented wave
SOC	Spin-Orbit Coupling
SCF	Self-Consistent Field
GGA	Generalized Gradient Approximation
PBE	Perdew, Burke and Ernzerhof functional 1996
PBEsol	PBE adapted for solids and surfaces (2008)
DOS	Density of state
CASTEP	Cambridge Serial Total Energy Package

Materials and properties

CB	Conduction Band
VB	Valence Band
CBM	Conduction Band Minimum
VBM	Valence Band Maximum
IP	Ionisation Potential
DSSC	Dye-Sensitized based Solar Cell
PSCs	Perovskite solar cell
SRH	Shockley-Read-Hall recombination

Photovoltaic

FF	Fill Factor
PCE	Power Conversion Efficiency
NREL	National Renewable Energy Laboratory
AM 1.5G	Air Mass 1.5 Global (solar spectrum)
SQ	Shockley-Queisser limit

List of symbols

α	Absorption coefficient
$m_{h,e}$	Carrier effective mass
μ	Carrier mobility
E_l	Deformation potential constant
D	Diffusion factor
L	Diffusion length
C_{ii}	Elastic constant,
$V_{xc}[n]$	Exchange and correlation potential
$V_{nucl}[n]$	External potential
$V_H[n]$	Hartree potential
∇^2	Laplacian
τ	Lifetime
P_{th}	Maximum theoretical power
V_{oc}	Open circuit voltage
$\mathrm{P_{out}}$	Output power produced by the solar cell
$\mathrm{P_{in}}$	Power of input light
η	Power conversion efficiency
$V(\vec{r},t)$	Potential
J_{SC}	Short circuit current density
$E_{\mathrm{tot}}[X]$	Total energy of the defective supercell
$E_{\mathrm{tot}}[\text{ bulk }]$	Total energy of the pristine bulk supercell
$\psi(\vec{r},t)$	Wave function

Contents

List of Figures

List of Tables

Introduction

Introduction

The world population is nearing 8 billion while energy demand is extensively increasing. The increased worldwide energy demand needs green and sustainable sources, which don't cause damages to our environment. The sun gives us more than enough of power to satisfy the entire world's energy demand. Solar energy is one of the most used renewable source of energy, readily available, and free with one limitation; our ability to directly convert the energy of light into electrical energy efficiently with an effective cost. The majority of devices used for this purpose nowadays are silicon based solar cells. This technology has been used since 1976. All these years were more than enough for scientist to understand this technology and develop an efficient strategy to improve the efficiency and reduce the cost. However, these cells are heavy and not flexible, too. While the monocrystalin silicon that needs a high technology and thus a high cost has no space for much improvement in power conversion efficiency (PCE).

In 2009, A. Kojima and collaborator [1] used, for the first time, organometal halide perovskites as visible-light sensitizers in dye-sensitized solar cell with PCE of 3 % . In 2012, Methylammonium Lead Iodide $MaPbI_3$ was used as a light harvester material for heterojunction mesoscopic with 9.7 % of PCE [2]. It was really a big step forward for an emerging material. Moreover, perovskite solar cells (PSCs) have very low production cost since they can be elaborated using low temperature solid solution process. Indeed, for these two reasons (low production cost as well as fast development in PCE) PSCs have attracted great attention in recent years. They may lead photovoltaic field in the future, due to their extraordinary optoelectronic properties such as high optical absorption, high mobility, and low non-radiative recombination rates ... etc [2–15]. In just few years, PSCs outperformed high production cost traditional photovoltaic technologies with high PCE of 26%. However, the organometallic perovskites are unstable, so their efficiency drops drastically, especially under humidity, light, and heat. Commercial application of these emerging materials has not yet started due to this instability and related issues [16–20]. The main challenge for many researchers nowadays is improving material's stability. Very recently, cesium has been reported to replace the sensitive to moisture and oxygen organic

cations MA and FA.

In this work, full inorganic perovskites is studied as alternative emerging materials. At the atomic level, and try to understand their high-performance, and improve their stability without losing in PCE.

This thesis is organized as follow: in the first chapter, we will first present photovoltaic system and discuss the link between PCE and internal parameters such as energy band gap, absorption, and mobility... etc. In the second part of this chapter, we will present perovskite materials by giving a brief description of their crystallographic structure and discussing geometrical stability factors. We present the excellent photovoltaic characteristics of these materials, too. In the second chapter, we give a brief introduction of simulation methods used in this work and provide a detailed description of point defects simulations using DFT method.

Results and discussions are presnted in the following three chapters. Chapter 3, presents our study when substituting the organic molecule by cesium atom for more stable material. Indeed, we investigate the structural stability, electronic, and optical properties as well as some carrier transport properties of full inorganic $CsPbI_3$ perovskites polymorphs. In chapter 4, we use solid solution by means of super-cell approach to partially or totally substitute iodide by bromine ($CsPbI_{3-x}Br_x$) in order to stabilize the preferred perovskite black phase, therefore, we investigate the stability as well as the electronic and optical characteristics of low symmetry orthorhombic structure. Meanwhile, this class of material has large diffusion length as well as high life time even in the presence of defects. The objective of last chapter is to give in depth understanding of defect chemistry of both $CsPbI_3$ and $CsPbBr_3$ perovskite through DFT method and finally conclusion and some perspectives.

Refrences

[1] Kojima, A.; Teshima, K.; Shirai, Y. and Miyasaka, T., May , (2009), **131**(17), 6050–6051.

[2] Kim, H.-S.; Lee, C.-R.; Im, J.-H.; Lee, K.-B.; Moehl, T.; Marchioro, A.; Moon, S.-J.; Humphry-Baker, R.; Yum, J.-H.; Moser, J. E.; Grätzel, M. and Park, N.-G., August , (2012), **2**.

[3] Lee, M. M.; Teuscher, J.; Miyasaka, T.; Murakami, T. N. and Snaith, H. J., November , (2012), **338**(6107), 643–647.

[4] Jeng, J.-Y.; Chiang, Y.-F.; Lee, M.-H.; Peng, S.-R.; Guo, T.-F.; Chen, P. and Wen, T.-C., *Advanced Materials*, 2013, **25**(27), 3727–3732.

[5] Liu, M.; Johnston, M. B. and Snaith, H. J., September , (2013), **501**(7467), 395–398.

[6] Snaith, H. J., November , (2013), **4**(21), 3623–3630.

[7] Liu, D. and Kelly, T. L., February , (2014), **8**(2), 133–138.

[8] Park, N.-G., March , (2015), **18**(2), 65–72.

[9] deQuilettes, D. W.; Vorpahl, S. M.; Stranks, S. D.; Nagaoka, H.; Eperon, G. E.; Ziffer, M. E.; Snaith, H. J. and Ginger, D. S., May , (2015), **348**(6235), 683–686.

[10] Yin, X.; Chen, P.; Que, M.; Xing, Y.; Que, W.; Niu, C. and Shao, J., March , (2016), **10**(3), 3630–3636.

[11] Sutton, R. J.; Eperon, G. E.; Miranda, L.; Parrott, E. S.; Kamino, B. A.; Patel, J. B.; Hörantner, M. T.; Johnston, M. B.; Haghighirad, A. A.; Moore, D. T. and Snaith, H. J., April , (2016), **6**(8), 1502458.

[12] Zhang, W.; Eperon, G. E. and Snaith, H. J., May , (2016), **1**(6), 1–8.

[13] Pedesseau, L.; Sapori, D.; Traore, B.; Robles, R.; Fang, H.-H.; Loi, M. A.; Tsai, H.; Nie, W.; Blancon, J.-C.; Neukirch, A.; Tretiak, S.; Mohite, A. D.; Katan, C.; Even, J. and Kepenekian, M., November , (2016), **10**(11), 9776–9786.

[14] Nia, N. Y.; Matteocci, F.; Cina, L. and DiCarlo, A., *ChemSusChem*, 2017, **10**(19), 3854–3860.

[15] Sanchez, S.; Christoph, N.; Grobety, B.; Phung, N.; Steiner, U.; Saliba, M. and Abate, A., October , (2018), **8**(30), 1802060.

[16] Wang, H.; Liu, H.; Li, W.; Zhu, L. and Chen, H., November , (2020), **77**, 105160.

[17] Xu, P., June , (2020), **132**(1), 74.

[18] Chen, M.; Ju, M.-G.; Garces, H. F.; Carl, A. D.; Ono, L. K.; Hawash, Z.; Zhang, Y.; Shen, T.; Qi, Y.; Grimm, R. L.; Pacifici, D.; Zeng, X. C.; Zhou, Y. and Padture, N. P., December , (2019), **10**(1).

[19] Becker, P.; Márquez, J. A.; Just, J.; Al-Ashouri, A.; Hages, C.; Hempel, H.; Jošt, M.; Albrecht, S.; Frahm, R. and Unold, T., April , (2019), page 1900555.

[20] Wang, K.; Jin, Z.; Liang, L.; Bian, H.; Bai, D.; Wang, H.; Zhang, J.; Wang, Q. and Liu, S., December , (2018), **9**(1).

1

Perovskite materials for Photovoltaic applications

1.1 Introduction

In this first chapter, we first briefly present the photovoltaic system by giving a short description of basic electrical characteristics such as power conversion efficiency PCE, short-circuit current and open-circuit voltage. Other internal parameters that directly affect PCE such as band gap, absorption, and mobility are also considered. In the second part, perovskite materials, their historical development, and crystallographic structure are introduced and both tolerance and octahedral factors are described. Finally, we will introduce hybrids and full inorganic perovskite solar cell materials, and their excellent characteristics are explained by showing their great potential to lead the next generation of photovoltaic devices.

1.2 Photovoltaic system

1.2.1 Generality

Solar cell is one of the key devices that are widely used to generate electricity from solar energy. In order to achieve this goal, semiconductors are used to absorb light. In general, energy conversion consists of the following stages: absorption of the photon, separation of charges (electron and holes), charges transport and finally collection of charges (Figure 1.1).

(i) Photon absorption: Sunlight has different wave lengths corresponding to different photon energies. Only photons with energy equal or greater than the material's band gap energy are absorbed causing the excitation of electrons from the valance band to the conduction band leaving a hole.

(ii) Separation of charges: The electrons and holes are separated and collected by electron transport material (ETM) and hole transport material (HTM) respectively.

(iii) Finally, charges transport, the previously generated charge carriers, must be extracted by an external circuit to do useful work.

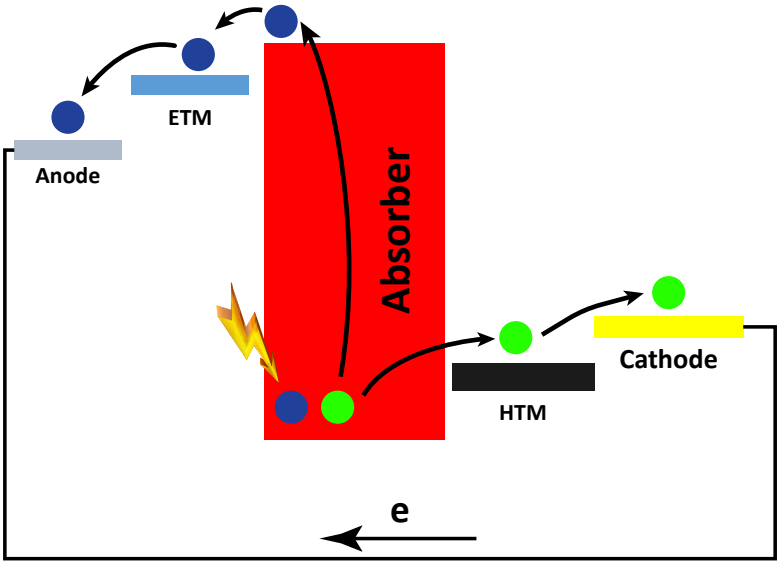

Figure 1.1: Schematic architecture of the working principle of a selective contact solar cell.

1.2.2 Solar cells generation

Solar cells are classified into three main categories (generations) depending on period of their development. The first generation is mainly made of conventional silicon pn-junction, which now dominate the photovoltaic market. This domination is caused by two biggest advantages: Silicon is very stable non-toxic material and one of the most abundant element on earth. Second is the long period of study (70 years). The optoelectronic and structural properties are very well understood. However, let's talk about the bad side, Si has an indirect bandgap and moderate absorption coefficient hence thick layers 300 μm are required to ensure sufficient photon absorption. Furthermore, two major silicon technologies were used in the photovoltaic field; the multi-crystalline silicon is fabricated with simple elaboration process and shows low production cost with low PCE of 10%. The alternative is the high pure mono-crystalline silicon (mono-Si) with PCE of 26%. Mono crystal means high production temperature (>1000C) and more advanced, and complex technology is needed, thus is much expensive. 2^{nd} Generation thin film corresponds to thin film solar cells, based on materials such as Copper Indium Gallium Selenide (CIGS) and Cadmium Telluride/Cadmium Sulphide (CdTe/CdS) they also include organic materials, with a few nanometres to tens of micrometres of thickness and hence can be flexible and able to growth on large areas. Due to simple preparation process they have much lower production

Table 1.1: Characteristic of different solar cells generation

1^{st} Generation	2^{nd} Generation	3^{rd} Generation
Highly efficient (> 20 %).	Low efficiency (around 10 %).	Highly efficient (>20 %).
Rather expensive (complex processes)	Low production cost	Very Low production cost
Very stable	Flexibility	Flexibility
		Not stable
		Toxic (lead based)

cost, but present a low conversion efficiency (10 to 20 %).

3^{rd} Generation solar cells include, Dye sensitized solar cells and hybrid organic inorganic solar cells... etc. The main goal is to get high PCE and low production cost, but they are still in the research stage and this novel technology is not commercially mature yet. Solar cells characteristics are summarized in Table 1.1.

1.2.3 Characterization

After the fabrication of the solar cell, power conversion efficiency should be evaluated and compared to other cells. Solar cells performance is evaluated under standard condition $25°C$, using artificial sunlight. PCE. or η, is the percentage of output power produced by the solar cell (P_{out}) to the power of input light (P_{in}). The last is standard e.g. $1kW = m^2$ for AM 1.5G spectrum, which simulates the global average of sun irradiation, including incidence angle, losses due to the absorption of sunlight in the atmosphere.
Hence:

$$\eta = \frac{\mathrm{P_{out}}}{\mathrm{P_{in}}} \tag{1.1}$$

For electronic device, power (P) is the product of current and potential. For solar cell, the two terms are multiplied by the Fill Factor (FF). In practice, when the photovoltaic cell is synthetized we measure and plot current-voltage (J-V) curve (see Figure 1.2). All characteristic of the solar cell could be extracted from this curve.

Where V_{oc} is the open circuit voltage (maximum potential difference obtained when the current is zero.), J_{SC} is the short circuit current density (voltage is zero when the cell is short circuited). Product of the two terms gives the maximum theoretical power P_{th}.

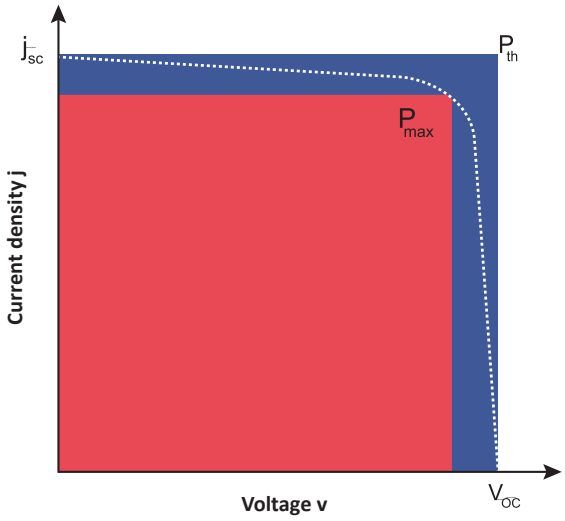

Figure 1.2: Current density voltage (J–V) curve.

FF given by:

$$\mathrm{FF} = \frac{\mathrm{P_{max}}}{\mathrm{P}_{th}} = \frac{\mathrm{P_{max}}}{\mathrm{V}_{OC}\,\mathrm{J}_{SC}} \tag{1.2}$$

PCE is given by

$$\eta = \frac{\mathrm{P_{max}}}{\mathrm{P_{in}}} = \frac{\mathrm{V_{OC}} \cdot J_{SC} \cdot FF}{\mathrm{P_{in}}} \tag{1.3}$$

One should keep in mind that PCE depends on external parameters such as cell area and incident light intensity, which are normalized in order to make meaningful comparison between cells. Moreover, the internal parameters such as: band gap energy, carrier mobilities, cell absorption and reflection coefficients... etc. are the main contributors to conversion efficiency.

1.2.4 Intrinsic properties of solar cell

As mentioned in the previous section, the most important parameter for each solar cell is PCE which is directly related to the Fill factor, open circuit voltage, and short circuit current. These three parameters are affected by many intrinsic factors namely: carrier diffusion length and lifetime, band gap, band alignment, defect density, recombination rate, carrier mobility and absorption coefficient... etc. Through Ab-initio calculations we able to determine several of these parameters. In the following sections, a brief introduction on these parameters is given.

1.2.4.1 Band gap

One of the most important parameters in solar cell is the gap energy, which is defined by the energy distance between the highest occupied level in the valence band and the lowest unoccupied level in the conduction band. In other words, the band gap represents the minimum required energy to excite an electron from the valence to the conduction band. According to Shockley-Queisser [1] (see Figure 1.3), this energy ranges from 1.1eV to 1.7eV for Single Junction (SJ) solar cells that could yield 33 % PCE which represents the maximum theoretical values for SJ solar cells.

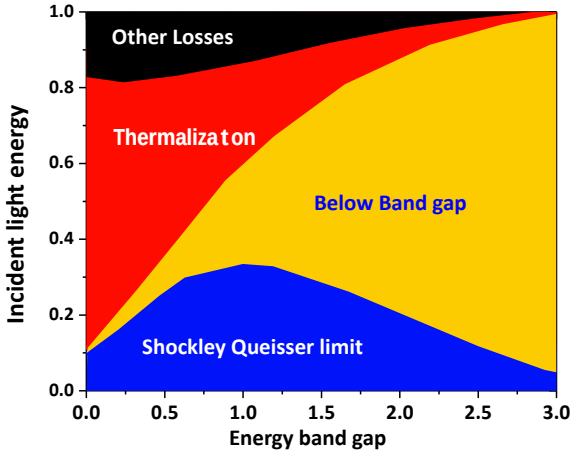

Figure 1.3: The Shockley–Queisser limit for the efficiency of single junction solar cell (Eg eV).

Moreover, if the semiconductor has lower band gap, excited electron by low energy, produce lower voltage. On the other side, if the band gap much larger, a smaller number of photons will be absorbed leading to a weaker current. Hence Eg should be tuned to get optimal value, which leads to the maximum efficiency.

1.2.4.2 Band alignment

The solar cell is formed by different materials (layers) (heterojunctions), i.e. absorber , hole transport material and electron transport material... etc. These layers don't have the same band gap. As result, discontinuities in the valence-band, and/or the conduction-band are formed. Many interactions are observed in the interface, thus limiting carrier transport.

In (Figure 1.4) different types of heterojunctions are presented.

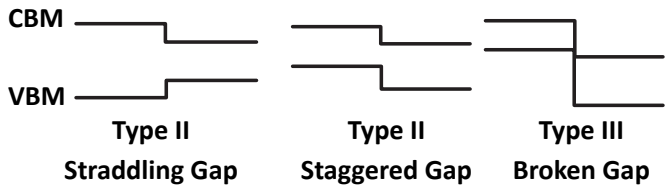

Figure 1.4: Schematic architecture of different types of heterojunctions in semiconductors.

For solar cell applications, energy bands should be aligned in order to allow electron and hole transport to ETM and HTM respectively. Indeed, CBM (VBM) of absorber should be higher (lower) than CBM(VBM) of ETM(HTM). This offset should be very small (0.2eV) to avoid the formation of large thermodynamic barrier at the heterojunction [2]. On the other hand, this barrier is used to block the transport of the electrons and holes in absorber/HTM and absorber/ETM contacts respectively. As presented in Figure1.5, band alignment has also much effect on Voc value.

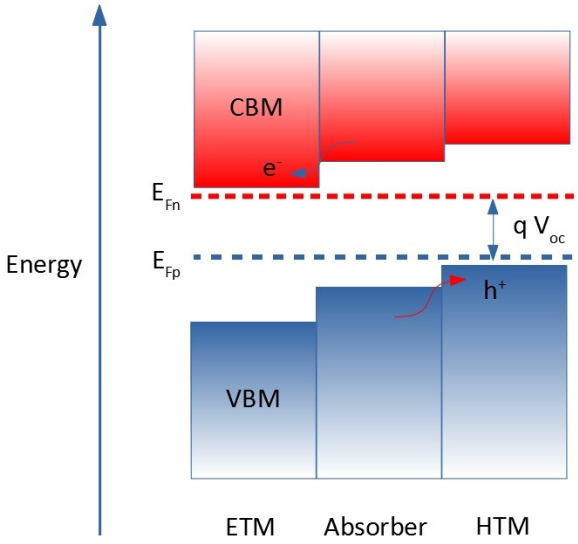

Figure 1.5: Schematic architecture of (ETM/Absorber/HTM) band alignment and their effect on open circuit voltage.

Therefore, before designing any photovoltaic cell, the first step is the determination of band position by selecting a suitable partner. The Figure 1.6, depicts the energy band

position of popular cell partners.

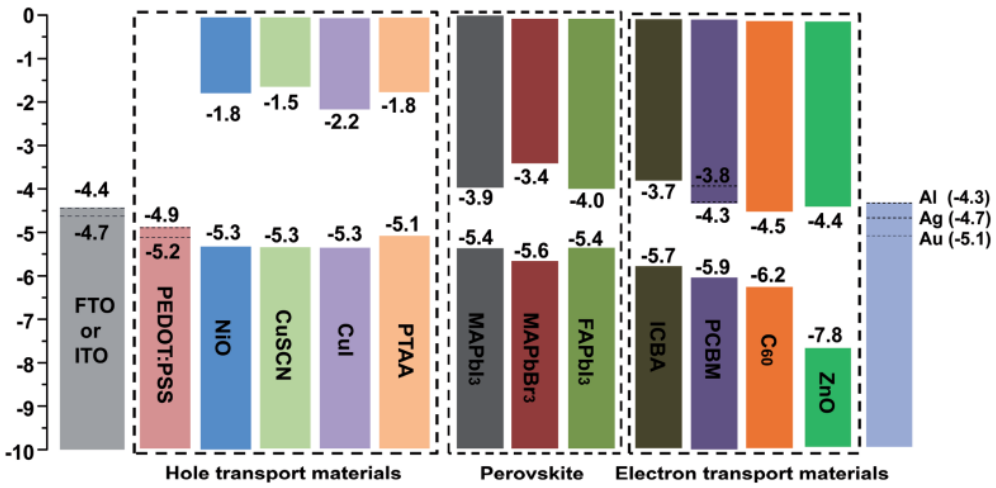

Figure 1.6: Band alignment of organometallic perovskite and commonly used materials in solar cells (eV). Reprinted with permission from Ref [3]

In the next chapter, we will give a detailed description on band alignment calculation through DFT method.

1.2.4.3 Absorption coefficient

The absorption coefficient α for a particular photon energy defines how much electromagnetic radiation can be absorbed by a material with a given thickness. Indeed, bandgap nature has a great effects on the absorption coefficient. For instance silicon has an indirect band gap that leads to a lower optical absorption coefficient ($10^3 cm^{-1}$) compared with GaAs ($10^5 cm^{-1}$) . Therefore, we need thicker layer when silicon is used in order to increase photon absorption.

1.2.4.4 Diffusion length and carrier lifetime

Diffusion length and lifetime of an electric carrier are the average length and time, respectively, between generation and recombination processes. They strongly depend on the type of recombination. Higher diffusion length means a longer lifetime. In the previous section, we said that we need thicker absorber, which is not very useful if the diffusion length is low because most generated carriers will recombine before reaching the ETM. The following

relation links these two physical quantities

$$L = \sqrt{D\tau} \tag{1.4}$$

Where L is Diffusion length, τ is lifetime and D is the diffusion factor which depends on the carrier mobility through Einstein's formula:

$$D = \frac{kT\mu}{e} \tag{1.5}$$

1.2.4.5 Recombination rate

The recombination rate is the ratio between excited and recombined carrier concentrations. The generated electrons lose energy to recombine with a hole and produce either heat or light. As presented in Figure 1.7, there are different recombination types; Shockley-Read-Hall, Radiative and Auger recombination. Shockley-Read-Hall SRH recombination is a

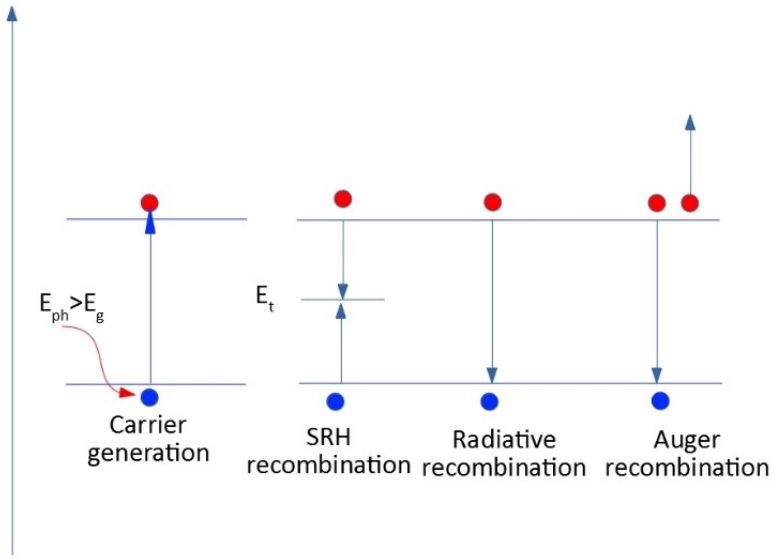

Figure 1.7: Schematic architecture of carrier recombination mechanisms in semiconductors after the generation.

process in two steps, first electron (or hole) is trapped in new energy level introduced by the defect, the trapped electron moves from trap level to the VB and recombines. The

energy difference Et-Ev (or Ec-Et in the other process) will be transferred to the crystal lattice or as a phonon emission.

Radiative recombination is dominant in direct band gap semiconductor. It is a recombination between an electron from CB and a hole from VB after this process a photon is generated.

Auger recombination process: an electron of CB recombines with a hole of the VB, an emitted energy will be given to an electron of CB, which thermalizes by going to the edge of the CB.

1.2.4.6 Defect tolerance

Generally, defects have profound impact on the performance of a material [4–9]. When defect doesn't have much effect on material properties the material is called defect tolerant. More precisely, this is the case when defects create shallow levels in the energy band gap rather than deep levels (recombination centre Figure 1.7) in the bandgap, for more detail on the point defect see chapter 2

1.2.4.7 Carrier mobility

One of the most important parameters for PCE is carrier mobility. It gives a measure of the charge carrier movement inside a material. It is directly related to effective mass through the following relation

$$\mu_{h,e} = \frac{q\tau}{2m_{h,e}} \tag{1.6}$$

Where $m_{h,e}$ is the carrier effective mass. Organometallic halide perovskites are characterised by low effective mass about 0.15 for both electron and hole. This is lower than traditional absorber like Si 1.06(0.59)[10] and higher than GaAs 0.067(0.44) [11] for electron (hole).

1.2.4.8 Exciton binding energy

After light absorption, electron-hole pair is generated. They interact with each other via long range Coulomb interaction giving birth to a new quasi-particle known as the exciton.

In other words, it is the energy required to disassociate the electron-hole pair. The exciton binding energy depends on dielectric constant. Two methods are proposed to calculate this parameter according to dielectric constant. If the material has a large dielectric constant the Coulomb interaction is reduced because the electric field is strongly screened and this is Wannier–Mott exciton case. The opposite is the Frenkel exciton. Due to their large dielectric constant and low effective masses, halide perovskite show very low exciton binding energy around 14 meV [12].

1.3 Perovskite materials and photovoltaic applications

In 2009 the first perovskite based solar cell (PSC) was born using liquid electrolyte perovskite in dye-sensitized solar cell (DSSC), the first obtained PCE was only 3% [13]. In 2012, Hui-Seon Kim and co-workers presented the first heterojunction mesoscopic solar cell with PCE of 9.7% using $MAPbI_3$ as a light harvester material [14]. Compared to other conventional solar cell materials, they provide the lowest cost in solar energy technology [14–17] with high power conversion efficiencies (PCE) approaching 24% [18]. Indeed, in just few years following their discovery, these materials outperformed Cadmium Telluride (CdTe) and not far from high-purity and high production cost crystalline silicon solar cell 26% [19]. The National Renewable Energy Laboratory (Colorado, United states) presents the confirmed PCE of different technology from 1976 to the present. Table 1.2 shows the last best research cells efficiencies for different photovoltaic.

Table 1.2: The last best research cells efficiencies for various photovoltaic technologies. Efficiencies confirmed by independent, recognized test labs [2021].

Solar cell technology	PCE	Developer name
Silicon	26.1	ISFH(Institute for Solar Energy Research Hamelin)
	22.3	FhG-ISE (Fraunhofer Institute for Solar Energy Systems)
	21.2	Solexel
GaAs	27.8	LG (LG Electronics)
	29.1	Alta device
CdTe	22.1	FirstSolar (First Solar Inc)
	25.2	KRICT/MIT (Korea Research Institute of Chemical Technology/ Massachusetts Institute of Technology)

In general, the most commonly used PSCs are the organic lead halide based materials of general formula ABX_3, where A is an organic monovalent cation like methylammonium (MA) or formamidinium (FA), B is an inorganic divalent cation like lead and X is a halogen anion (I, Br, Cl or F). The organometallic perovskite are unstable and after few hours of use, their efficiency decreases drastically, especially under humidity and heat. The main challenge for many researchers nowadays is improving material's stability. Recently, Cesium has been reported to replace the sensitive to moisture and oxygen organic cations MA and FA. Indeed, Cs+ (1.67 Å) cation has a smaller ionic radius than MA+ (1.80 Å) or FA+ (1.90 Å) with Goldschmidt tolerance factor of 0.81 [20, 21]. Actually, fully inorganic cesium lead iodide perovskite $CsPbI_3$ has been much studied owing to its higher thermal stability[22–28] and high PCE of 13.4% for quantum dot devices [24] and 15.1 % for a thin films [23]. In the Table 1.3, I present both internal and external characteristic of perovskite material compared with other widely used conventional solar cell material.

Table 1.3: Internal and external characteristic of PSCs thin film compared with conventional Si (crystalline cell) and GaAs (thin film cell).

Characteristic	Perovskite [29]	Conventional	
		Si [19]	GaAs[30]
FF	84.8	84.9	86.7
Voc (V)	1.1805	0.738	1.1272
Jsc (mA/cm2)	25.14	42.65	29.78
PCE (%)	25.2 ± 0.8	26.7 ± 0.5	29.1 ± 0.6
Effective mass me(mh)	0.15	1.06(0.59)[10]	0.067(0.44)[11]
Gap (eV)	Direct, tunable 1.1–2.5	Indirect 1.14	Direct 1.43
Absorption coefficient (cm–1)	greater than 10^5	10^3	10^5
Exciton binding energy (meV)	around 14 [12]	About 10 [31]	4.2 [11]

1.3.1 Perovskite materials

The perovskite calcium titanium oxide ($CaTiO_3$) mineral was discovered in the Ural Mountains of Russia by Gustav Rose in 1839 and is named after Russian mineralogist Lev Alekseevich Perovski (1972–1856). Today this name is also applied to compounds with general chemical formula ABX_3 having a similar crystallographic structure such as $CaTiO_3$. These compounds have attracted much attention due to their interesting physical properties, such as ferroelectric, superconductivity, catalysis and other optoelectronic properties [32–39].

This makes them desirable for various technological applications. The most important application for us is the solar energy conversion.

1.3.1.1 Crystal structure

The ideal perovskite should have the same crystallographic structure as $CaTiO_3$ mineral, consisting of corner-sharing BX_6 octahedra in the three directions, the cuboctahedral cavity in each unit cell is occupied by A atom forming cuboctaheral geometry AX_{12} (see Figure 1.8). The same crystal structure is also found for a wide range of materials with ABX_3 stoichiometry[40].

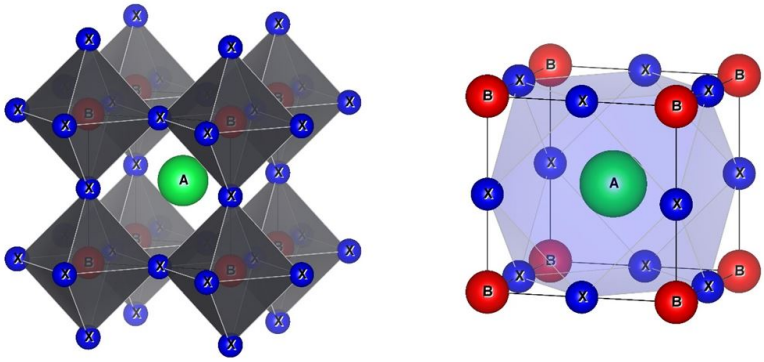

Figure 1.8: Ideal perovskite structure, BX_6 octahedral corner sharing (left) and cuboctahedral AX_{12} geometry (right).

These materials are the archetypal systems for phase transitions with accessible cubic, tetragonal, orthorhombic, trigonal and monoclinic polymorphs depending on the degree of tilting and rotation of the BX_6 octahedra in the lattice[40–43].

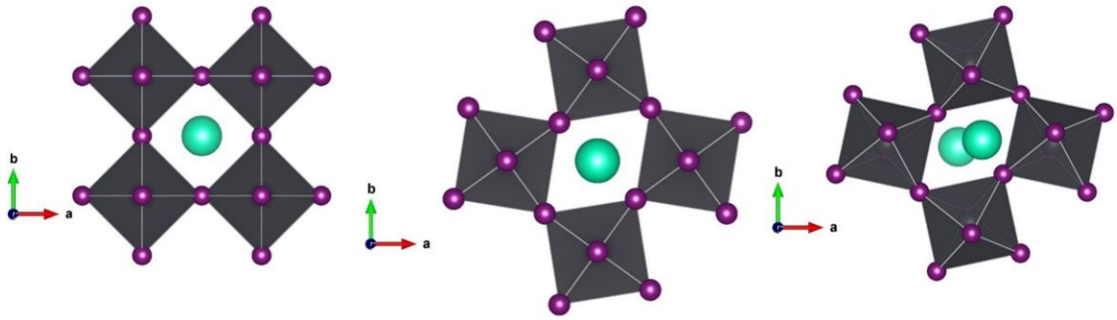

Figure 1.9: Tilting of the BX_6 octahedra in the cubic, tetragonal and orthorhombic perovskite.

1.3.1.2 Goldschmidt and octahedral Factors

As we said in the previous section, perovskite take many phases, Goldschmidt [44] proposed a tolerance factor (TF) to estimate the distortion degree and predict the stability of perovskite structure. This factor is based on the ratio of the ionic radii [45] of its constituent using a simple geometrical principles where, atoms are considered as a collection of rigid spheres:

$$t = \frac{r_A + r_X}{\sqrt{2}\,(r_B + r_X)} \tag{1.7}$$

Here r_A, r_B and r_X are the ionic radius of A-cation B-cation and X anion respectively. For the ideal cubic perovskite $r_A + r_X = \sqrt{2}(r_B + r_X)$. For distorted perovskite, the octahedra will tilt in order to fill the available space. Disorder perovskite structures as well as ideal structure have the following tolerance factors (TF) [40].

0.71-0.9	0.9-1	>1
Orthorhombic/Rhombohedral	Cubic	Hexagonal or Tetragonal

The TF alone is not sufficient for the prediction of perovskite structures. Other condition should be satisfied. The B cation is six fold coordinated to X anions, therefore, it should have the appropriate size to fit into the octahedral void formed by the six X anions. From a pure geometric consideration, the minimum radius for the B-cation is 0.414 r_X. To estimate the fit of B into X_6 octahedron, the octahedral factor μ is defined as follows:

$$\mu = \frac{r_B}{r_X} \tag{1.8}$$

Based on these two factors, we are now able to identify the stability range, using t and μ limits [46–50].

(i) Stretch limit

If the A cation is so large and touches all twelve X anions (t =1). This is the case of ideal perovskite. SL boundary.

(ii) Octahedral limit

Two X anions in the same octahedron are in contact, the distance satisfy the following

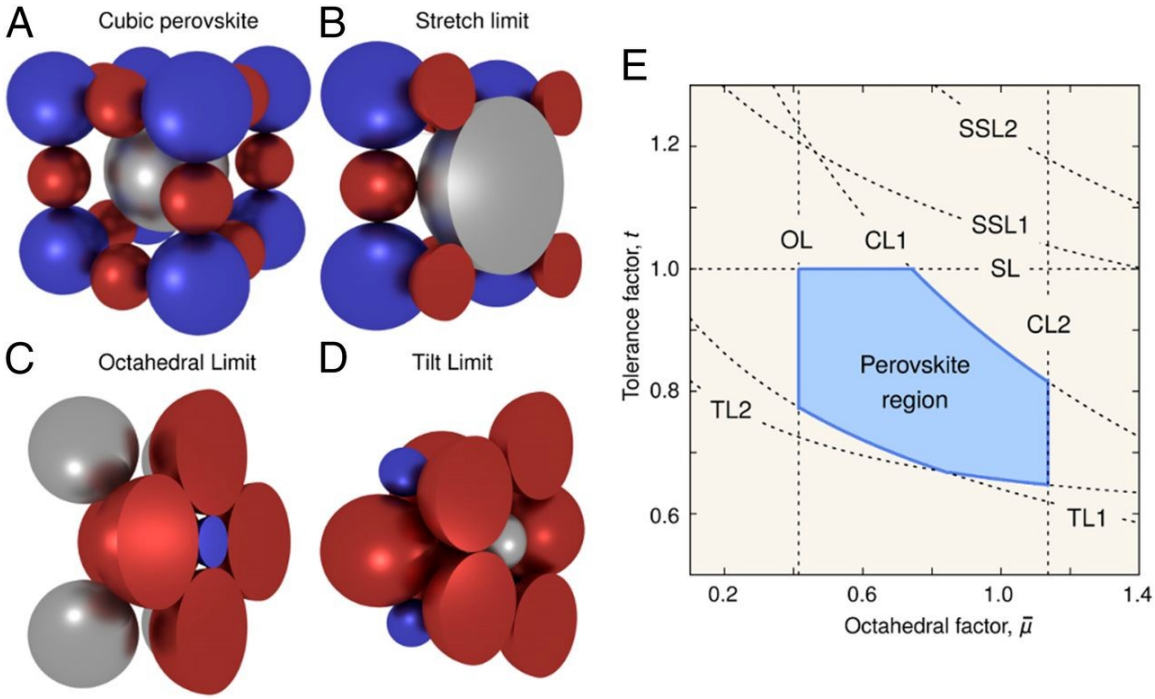

Figure 1.10: Perovskite stability region. Reprinted from Ref [46]. Copyright (2018) National Academy of Sciences of the united states of America.

condition $\sqrt{2}(r_b + r_x) = 2r_x$ and thus $\mu \geq \sqrt{2} - 1$

(iii) Tilt limits

When the octahedral cavity is bigger than the A-site, BX_6 octahedra tilt and get distorted and thus the coordination of A-site is reduced. We label this bound by tilt limit (TL). In Table 1.4, we summarise the tolerance and octahedral factor for some halide perovskites material.

Table 1.4: List of some halide perovskite ABX_3 compounds and their tolerance and octahedral factors.

Compound	Ionic radius			TF	OF
	r_A [21, 51]	r_B[51]	r_X [52]		
$MAPbI_3$	2.17	1.03	2.2	0.96	0.47
$MAPbCl_3$	2.16	0.99	1.81	1.00	0.55
$MAPbBr_3$	2.16	0.98	1.96	0.99	0.5
$FAPbI_3$	2.53	1.03	2.2	1.04	0.47
$FAPbCl_3$	2.53	0.99	1.81	1.10	0.55
$FAPbBr_3$	2.53	0.98	1.96	1.08	0.5
$CsPbI_3$	1.88	1.03	2.2	0.90	0.48
$CsPbCl_3$	1.88	0.99	1.81	0.93	0.55
$CsPbBr_3$	1.88	0.98	1.96	0.92	0.5

All presented compounds verify both octahedral and tolerance factors and experimen-

tally synthesised on their perovskite structure.

1.3.2 Fabrication

After the first use of full perovskite as solar absorber materials many thin film deposition techniques have been developed to fabricate perovskite film such as rapid deposition crystallization, Vapour assisted solution processing, Thermal evaporation, Pulse laser deposition, Electrospray-assisted deposition. But the most widely used technique due to its simplicity and thus the low-cost requirement are: Single-step deposition and Two-step sequential deposition. In the Figure 1.11, we gives a schematic representation of these last two techniques.

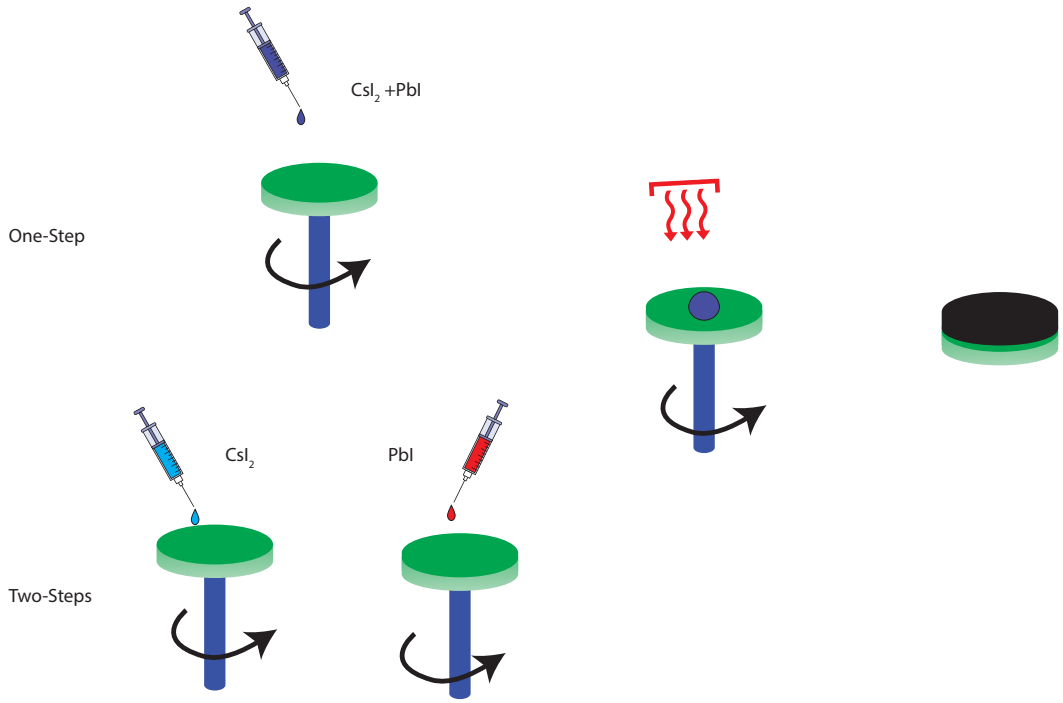

Figure 1.11: Schematic representation of Single-step and Two-Steps deposition techniques.

In the following as example, we present the synthesis procedure of $CsPbI_3$ perovskite absorber solar cell through a simple deposition method given by Ref [53]. The preparation of substrate -most used is Fluorine doped Tin Oxide (FTO)-coated glass substrates and after, the deposition also with spin coating method (i) the inorganic TiO_2 as electron transport layer, (ii) perovskite as absorber and (iii) organic hole transport layer suquestly

and finally silver or gold electrodes are then deposed using thermal evaporation method. In Table 1.5, we present the detailed information of each fabrication stage.

Table 1.5: $CsPbI_3$ PSCs deposition procedures given by Ref [53] as well as the different possible material for ETL, HTL and electrode.

Layer	Procedure [53]	Condition [53]	Layer Thickness [53]	Other possible partner
Substrate	FTO-coated glass substrates are first etched by HCl and Zinc powder and cleaned.			
ETL	From the titanium isopropoxide in anhydrous ethanol, Inorganic compact and mesoporous layer TiO2 are spin coates as on FTO substrate	2000 rpm for 60 s	230nm-400 nm	Metal oxide: TiO2 [54–57], Al2O3 [15, 58], ZnO [58] SnO2[59] Organic molecules: Fullerenes [60, 61]
Perovskite layer	The precursor solution of PbI2 and CsI are prepared and deposited by spin-coating (room-temperature) onto the last prepared FTO substrates with TiO2 layer and annealed (350C) to form a pure phase to kep this phase device rapidly cooled at room temperature	500 rpm for 10 followed by 1500 rpm for 20 s	200 nm - 400 nm	MAPbI3, FAPbI3, $CsPbBr_3$
HTL	From a 0.08 M solution of SpiroOMeTAD, Pre-oxidised SpiroOMeTAD organic charge transport layer are spin coated.	2000 rpm		Metal oxide: CoOx[62], CrOx [63], NiOx [64–67], Organic: Polymer [68, 69]
Electrode	80 to 120 nm of silver, or 20 nm of gold followed by 120 nm of silver were deposed using thermal evaporation method.		120-140 nm	Carbon[70]

1.3.3 Perovskite solar cell architecture

As we said, the first adaptations of perovskite material ($MAPbI_3$ and $MAPbBr_3$) were in solar cell application as a liquid electrolyte in dye-sensitized solar cell DSSC with PCE of 3% [13]. Moreover, to enhance the stability as well as efficiency numerous investigations have been carried out. Solar cell are formed by different components according to their type and arrangement. Several structures have been reported: Regular planar structure, Inverter planar structure and Mesoporous structure.

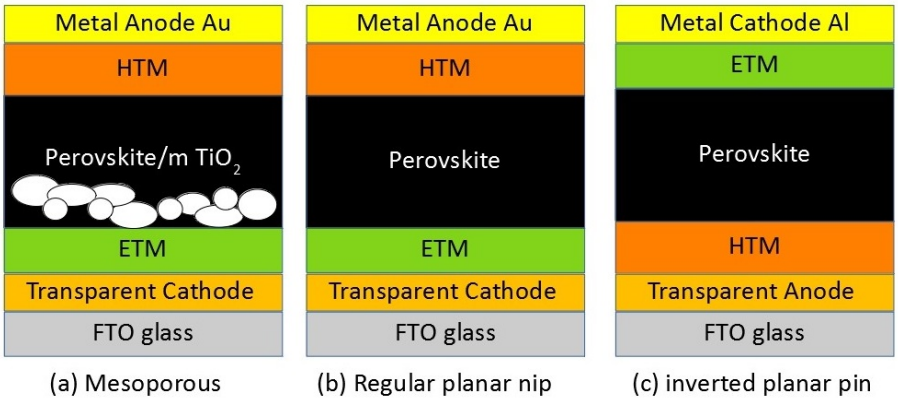

Figure 1.12: Schematic diagrams of different perovskite solar cell architecture.

1.3.4 Challenges

PSC is the future of the solar cell due to its fast progress in PCE from 3% to 26% in a short period. However, a huge challenge related to the stability issue blocks commercial application of this emerging material. There are three main drawbacks: stability, toxicity and scalability. In the next figure, we summarized the commercialization issue of PSCs.

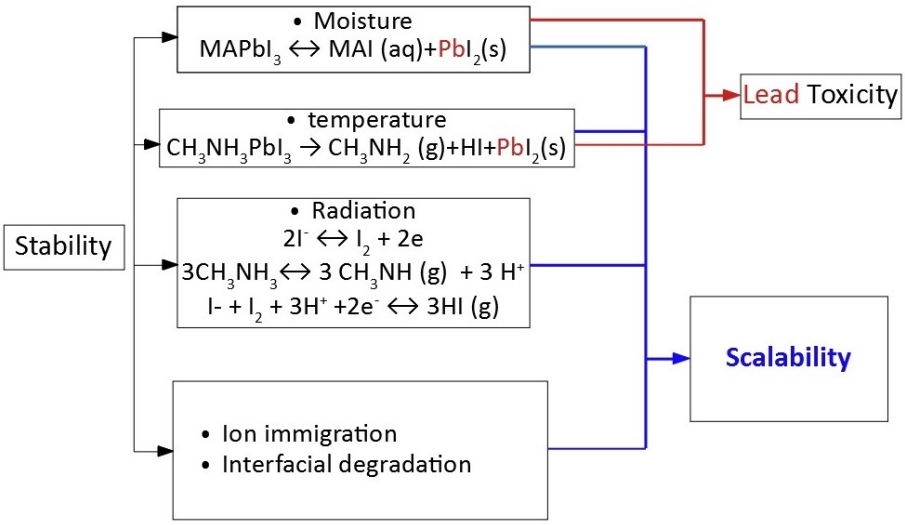

Figure 1.13: Representation of the biggest commercialization issue of perovskite solar cells technologies.

From this figure, it is clear that all PCSs issues are directly related to the stability of perovskite material.

Refrences

[1] Shockley, W. and Queisser, H. J., March , (1961), **32**(3), 510–519.

[2] Xu, P., June , (2020), **132**(1), 74.

[3] Bai, Y.; Meng, X. and Yang, S., *Advanced Energy Materials*, 2018, **8**(5), 1701883.

[4] Adinolfi, V.; Yuan, M.; Comin, R.; Thibau, E. S.; Shi, D.; Saidaminov, M. I.; Kanjanaboos, P.; Kopilovic, D.; Hoogland, S.; Lu, Z.-H.; Bakr, O. M. and Sargent, E. H., *Advanced Materials (Deerfield Beach, Fla.)*, 2016, **28**(17), 3406–3410.

[5] Chen, Y.; Yi, H. T.; Wu, X.; Haroldson, R.; Gartstein, Y. N.; Rodionov, Y. I.; Tikhonov, K. S.; Zakhidov, A.; Zhu, X.-Y. and Podzorov, V., August , (2016), **7**(1), 12253.

[6] Leijtens, T.; Eperon, G. E.; Barker, A. J.; Grancini, G.; Zhang, W.; Ball, J. M.; Kandada, A. R. S.; Snaith, H. J. and Petrozza, A., November , (2016), **9**(11), 3472–3481.

[7] deQuilettes, D. W.; Vorpahl, S. M.; Stranks, S. D.; Nagaoka, H.; Eperon, G. E.; Ziffer, M. E.; Snaith, H. J. and Ginger, D. S., May , (2015), **348**(6235), 683–686.

[8] Meggiolaro, D.; Motti, S. G.; Mosconi, E.; Barker, A. J.; Ball, J.; Perini, C. A. R.; Deschler, F.; Petrozza, A. and Angelis, F. D., March , (2018), **11**(3), 702–713.

[9] Kang, J. and Wang, L.-W., January , (2017), **8**(2), 489–493.

[10] Green, M. A., March , (1990), **67**(6), 2944–2954.

[11] Sell, D. D.; Stokowski, S. E.; Dingle, R. and DiLorenzo, J. V., May , (1973), **7**(10), 4568–4586.

[12] Ruf, F.; Aygüler, M. F.; Giesbrecht, N.; Rendenbach, B.; Magin, A.; Docampo, P.; Kalt, H. and Hetterich, M., March , (2019), **7**(3), 031113.

[13] Kojima, A.; Teshima, K.; Shirai, Y. and Miyasaka, T., May , (2009), **131**(17), 6050–6051.

[14] Kim, H.-S.; Lee, C.-R.; Im, J.-H.; Lee, K.-B.; Moehl, T.; Marchioro, A.; Moon, S.-J.; Humphry-Baker, R.; Yum, J.-H.; Moser, J. E.; Grätzel, M. and Park, N.-G., August , (2012), **2**.

[15] Lee, M. M.; Teuscher, J.; Miyasaka, T.; Murakami, T. N. and Snaith, H. J., November , (2012), **338**(6107), 643–647.

[16] Snaith, H. J., November , (2013), **4**(21), 3623–3630.

[17] Katan, C.; Mercier, N. and Even, J., March , (2019), **119**(5), 3140–3192.

[18] Jeon, N. J.; Na, H.; Jung, E. H.; Yang, T.-Y.; Lee, Y. G.; Kim, G.; Shin, H.-W.; Il Seok, S.; Lee, J. and Seo, J., August , (2018), **3**(8), 682–689.

[19] Yoshikawa, K.; Kawasaki, H.; Yoshida, W.; Irie, T.; Konishi, K.; Nakano, K.; Uto, T.; Adachi, D.; Kanematsu, M.; Uzu, H. and Yamamoto, K., May , (2017), **2**(5).

[20] Saliba, M.; Matsui, T.; Domanski, K.; Seo, J.-Y.; Ummadisingu, A.; Zakeeruddin, S. M.; Correa-Baena, J.-P.; Tress, W. R.; Abate, A.; Hagfeldt, A. and Gratzel, M.,

October , (2016), **354**(6309), 206–209.

[21] Kieslich, G.; Sun, S. and Cheetham, A. K., *Chem. Sci.*, 2014, **5**(12), 4712–4715.

[22] Sutton, R. J.; Filip, M. R.; Haghighirad, A. A.; Sakai, N.; Wenger, B.; Giustino, F. and Snaith, H. J., August , (2018), **3**(8), 1787–1794.

[23] Wang, K.; Jin, Z.; Liang, L.; Bian, H.; Bai, D.; Wang, H.; Zhang, J.; Wang, Q. and Liu, S., December , (2018), **9**(1).

[24] Sanehira, E. M.; Marshall, A. R.; Christians, J. A.; Harvey, S. P.; Ciesielski, P. N.; Wheeler, L. M.; Schulz, P.; Lin, L. Y.; Beard, M. C. and Luther, J. M., October , (2017), **3**(10), eaao4204.

[25] Sanchez, S.; Christoph, N.; Grobety, B.; Phung, N.; Steiner, U.; Saliba, M. and Abate, A., October , (2018), **8**(30), 1802060.

[26] Becker, P.; Márquez, J. A.; Just, J.; Al-Ashouri, A.; Hages, C.; Hempel, H.; Jošt, M.; Albrecht, S.; Frahm, R. and Unold, T., April , (2019), page 1900555.

[27] Eperon, G. E.; Paternò, G. M.; Sutton, R. J.; Zampetti, A.; Haghighirad, A. A.; Cacialli, F. and Snaith, H. J., *Journal of Materials Chemistry A*, 2015, **3**(39), 19688–19695.

[28] Kulbak, M.; Gupta, S.; Kedem, N.; Levine, I.; Bendikov, T.; Hodes, G. and Cahen, D., January , (2016), **7**(1), 167–172.

[29] Jung, E. H.; Jeon, N. J.; Park, E. Y.; Moon, C. S.; Shin, T. J.; Yang, T.-Y.; Noh, J. H. and Seo, J., March , (2019), **567**(7749), 511–515.

[30] Green, M. A.; Dunlop, E. D.; Hohl-Ebinger, J.; Yoshita, M.; Kopidakis, N. and Hao, X., *Progress in Photovoltaics: Research and Applications*, 2020, **28**(7), 629–638.

[31] Macfarlane, G. G.; McLean, T. P.; Quarrington, J. E. and Roberts, V., January , (1959), **8**, 388–392.

[32] Navrotsky, A., June , (1999), **284**(5421), 1788–1789.

[33] Suntivich, J.; May, K. J.; Gasteiger, H. A.; Goodenough, J. B. and Shao-Horn, Y., December , (2011), **334**(6061), 1383–1385.

[34] Mundy, J. A.; Brooks, C. M.; Holtz, M. E.; Moyer, J. A.; Das, H.; Rébola, A. F.; Heron, J. T.; Clarkson, J. D.; Disseler, S. M.; Liu, Z.; Farhan, A.; Held, R.; Hovden, R.; Padgett, E.; Mao, Q.; Paik, H.; Misra, R.; Kourkoutis, L. F.; Arenholz, E.; Scholl, A.; Borchers, J. A.; Ratcliff, W. D.; Ramesh, R.; Fennie, C. J.; Schiffer, P.; Muller, D. A. and Schlom, D. G., September , (2016), **537**(7621), 523–527.

[35] Tan, Z.-K.; Moghaddam, R. S.; Lai, M. L.; Docampo, P.; Higler, R.; Deschler, F.; Price, M.; Sadhanala, A.; Pazos, L. M.; Credgington, D.; Hanusch, F.; Bein, T.; Snaith, H. J. and Friend, R. H., September , (2014), **9**(9), 687–692.

[36] Loudon, J. C.; Mathur, N. D. and Midgley, P. A., December , (2002), **420**(6917), 797–800.

[37] Park, J.-H.; Vescovo, E.; Kim, H.-J.; Kwon, C.; Ramesh, R. and Venkatesan, T., April , (1998), **392**(6678), 794–796.

[38] Zhang, W.; Eperon, G. E. and Snaith, H. J., May , (2016), **1**(6), 1–8.

[39] Bednorz, J. G. and Müller, K. A., June , (1986), **64**(2), 189–193.

[40] Lufaso, M. W. and Woodward, P. M., December , (2001), **57**(6), 725–738.

[41] Woodward, P. M., February , (1997), **53**(1), 44–66.

[42] Woodward, P. M., February , (1997), **53**(1), 32–43.

[43] Glazer, A. M., November , (1972), **28**(11), 3384–3392.

[44] Goldschmidt, V. M., May , (1926), **14**(21), 477–485.

[45] Shannon, R. D., September , (1976), **32**(5), 751–767.

[46] Filip, M. R. and Giustino, F., May , (2018), **115**(21), 5397–5402.

[47] Li, C.; Soh, K. C. K. and Wu, P., June , (2004), **372**(1), 40–48.

[48] Li, C.; Lu, X.; Ding, W.; Feng, L.; Gao, Y. and Guo, Z., December , (2008), **64**(6), 702–707.

[49] Pilania, G.; Balachandran, P. V.; Kim, C. and Lookman, T., *Frontiers in Materials*, 2016, **3**.

[50] Giaquinta, D. M. and Loye, H.-C. z., Structural Predictions in the ABO3 Phase Diagram, 2002.

[51] Travis, W.; Glover, E. N. K.; Bronstein, H.; Scanlon, D. O. and Palgrave, R. G., *Chemical Science*, 2016, **7**(7), 4548–4556.

[52] Park, N.-G., March , (2015), **18**(2), 65–72.

[53] Sutton, R. J. *Towards Stable Perovskite Materials for Photovoltaics* Doctor of Philosophy Thesis, August , (2018).

[54] Li, J.-F.; Zhang, Z.-L.; Gao, H.-P.; Zhang, Y. and Mao, Y.-L., September , (2015), **3**(38), 19476–19482.

[55] Lee, J.-W.; Lee, S. H.; Ko, H.-S.; Kwon, J.; Park, J. H.; Kang, S. M.; Ahn, N.; Choi, M.; Kim, J. K. and Park, N.-G., April , (2015), **3**(17), 9179–9186.

[56] Lee, J.-W.; Lee, T.-Y.; Yoo, P. J.; Grätzel, M.; Mhaisalkar, S. and Park, N.-G., May , (2014), **2**(24), 9251–9259.

[57] Mali, S. S.; Shim, C. S.; Park, H. K.; Heo, J.; Patil, P. S. and Hong, C. K., March , (2015), **27**(5), 1541–1551.

[58] Zhang, J.; Hultqvist, A.; Zhang, T.; Jiang, L.; Ruan, C.; Yang, L.; Cheng, Y.; Edoff, M. and Johansson, E. M. J., *ChemSusChem*, 2017, **10**(19), 3810–3817.

[59] Song, J.; Zheng, E.; Bian, J.; Wang, X.-F.; Tian, W.; Sanehira, Y. and Miyasaka, T., May , (2015), **3**(20), 10837–10844.

[60] Jeng, J.-Y.; Chiang, Y.-F.; Lee, M.-H.; Peng, S.-R.; Guo, T.-F.; Chen, P. and Wen, T.-C., *Advanced Materials*, 2013, **25**(27), 3727–3732.

[61] Liang, P.-W.; Chueh, C.-C.; Williams, S. T. and Jen, A. K.-Y., *Advanced Energy Materials*, 2015, **5**(10), 1402321.

[62] Shalan, A. E.; Oshikiri, T.; Narra, S.; Elshanawany, M. M.; Ueno, K.; Wu, H.-P.; Nakamura, K.; Shi, X.; Diau, E. W.-G. and Misawa, H., December , (2016), **8**(49),

33592–33600.

[63] Wang, M.; Tang, Q.; An, J.; Xie, F.; Chen, J.; Zheng, S.; Wong, K. Y.; Miao, Q. and Xu, J., October , (2010), **2**(10), 2699–2702.

[64] Xu, X.; Liu, Z.; Zuo, Z.; Zhang, M.; Zhao, Z.; Shen, Y.; Zhou, H.; Chen, Q.; Yang, Y. and Wang, M., April , (2015), **15**(4), 2402–2408.

[65] Cao, K.; Zuo, Z.; Cui, J.; Shen, Y.; Moehl, T.; Zakeeruddin, S. M.; Grätzel, M. and Wang, M., October , (2015), **17**, 171–179.

[66] Xie, F.; Chen, C.-C.; Wu, Y.; Li, X.; Cai, M.; Liu, X.; Yang, X. and Han, L., September , (2017), **10**(9), 1942–1949.

[67] Yin, X.; Chen, P.; Que, M.; Xing, Y.; Que, W.; Niu, C. and Shao, J., March , (2016), **10**(3), 3630–3636.

[68] Nia, N. Y.; Matteocci, F.; Cina, L. and DiCarlo, A., *ChemSusChem*, 2017, **10**(19), 3854–3860.

[69] Lin, Q.; Jiang, W.; Zhang, S.; Nagiri, R. C. R.; Jin, H.; Burn, P. L. and Meredith, P., March , (2017), **9**(10), 9096–9101.

[70] Jeon, I.; Seo, S.; Sato, Y.; Delacou, C.; Anisimov, A.; Suenaga, K.; Kauppinen, E. I.; Maruyama, S. and Matsuo, Y., November , (2017), **121**(46), 25743–25749.

2

Theory and Computational Methodology

2.1 Introduction

The resolve of the basic equation in quantum mechanics “Schrodinger equation” for a given material gives us an enormous opportunity to understand its fundamental properties. The purpose of the first part of this chapter is to give a short and brief presentation of the Density Functional Theory (DFT) and pseudo potential plane wave (PPPW) method. In the second part, I give a description on computational methodology by explaining the electronic structure and how it can be used to extract a useful information about studied system such as band alignment, carrier effective mass as well as carrier mobility and other related quantities. In the last part, I intend to provide a detailed description of point defects simulations using the above-mentioned method (DFT-PPPW).

2.2 Theoretical background

In 1925 Erwin Schrödinger postulated his equation, which is a linear equation of the wave function of a quantum-mechanical system, which describes their variation in the space and time.

$$i\frac{\partial}{\partial t}\psi(\vec{r},t) = \left[\frac{-1}{2}\nabla^2 + V(\vec{r},t)\right]\psi(\vec{r},t) \tag{2.1}$$

Where ∇^2 the Laplacian, $\vec{r}$ is the position eigenvector and $V(\vec{r},t)$ is the potential.

Indeed, all properties of a quantum system; atom, molecule or a solid are determined by their wave function $\psi(\vec{r},t)$ and corresponding energy and their derivatives. Nevertheless, exact solution of this problem is only possible for few simple systems such as the hydrogen atom, free electron, and harmonic oscillator. In this thesis, we use time independent Schrodinger equation 2.2.

$$\left[-\frac{1}{2}\nabla^2 + V(\vec{r})\right]\psi(\vec{r}) = E\psi(\vec{r}) \tag{2.2}$$

Where E is the energy.

As we mentioned above, the exact solution is impossible for the multi particle sys-

tem, and therefore, approximation should be used. First, since the nuclei are much heavier than electrons and thus they move much slower than the electrons, their movement can be separated, this is Born and Oppenheimer approximation[1]. However, the problem is not yet solved. In 1927 Hartree propose to separate electrons and write the wave function as a product of many electronic system. In 1930, Vladimir Aleksandrovich Fock and John Clarke Slater treated the wave function as Slater determinant, which includes the antisymmetric property of the wave function and respects the exclusion principle of Pauli.

2.2.1 Density Functional Theory

Hartree fock method was used to resolve Schrodinger equation for molecules but failed for more complicated system for the following reasons: it ignores electronic correlation energy part so doesn't gives the real wave function and exact energy and it is also very expensive method (long time, high memory). Density-functional theory (DFT) was developed to solve these issues by giving us a practical way to solve Schrodinger equation for complicated system by using the electron density as a basic source to get information on an electronic system (Thomas and Fermi 1920). Indeed, DFT found enormous success in physics, chemistry and materials science, which provides a description of material at the atomic scale. In this section, we will briefly introduce this method.

Hohenberg and Kohn (HK) [2] in 1964 came up with the following two basis theorems of DFT: The first theorem states that the external potential $V_{ext(r)}$ uniquely determines the wave function and as consequent determine the electronic density. Hohenberg and Kohn have proven that $V_{ext(r)}$ is uniquely determined by the density $n(r)$. 2^{nd} the exact ground state density is a unique functional of the minimum energy (ground state energy). Until this point, the form of this functional is not yet known. In following year Kohn and Sham [3] provided an approach to compute this and gave the following equation 2.3 known as Kohn-Shame (KS) equation:

$$\left[-\frac{1}{2}\nabla^2 + V_{nucl}[n] + V_H[n] + V_{xc}[n]\right]\psi(\vec{r}) = \varepsilon\psi(\vec{r}) \tag{2.3}$$

Where they replaced the interacting electronic system by a non-interacting one with the same density as well as the same ground total energy, and put all the difference in the exchange and correlation potential $V_{xc}[n]$. In above equation $-\frac{1}{2}\nabla^2$ is the kinetic energy potential, $V_H[n]$ the Hartree potential, $V_{nucl}[n]$ is the external potential on the electronic system that created by the nuclei.

Until this point DFT is an exact theory where it is simple to calculate the kinetic energy of the non-interacting system, is also simple to calculate Hartree potential and the potential applied by the nucleus. The difficult part until this day is $V_{xc}[n]$. Approximations have been made to solve this issue such as Local Density Approximations (LDA)[4] Generalized-Gradient Approximation (GGA)[5, 6], Hybrid functional[7] ...etc.

KS equation is then solved by an iterative way through the variational principle depicted in the following chart:

In this work, and in order to calculate the physical properties, I use the pseudo- potential plane wave (PPPW) method.

2.2.1.1 Pseudopotential

Only the valence electrons are chemically active and most of the properties of a solid are related to the valence electrons. Therefore, we can replace the effect of the core electrons on a valence system by a pseudo potential. In other words, we replace the complicated interactions between core electrons of a physical system by pseudo potential.

2.2.1.2 Plane Wave Basis Sets

In order to solve KS equation we should expand the wave functions ψ in a specific basis set. The plane wave basis set is the most used one for many DFT codes such as VASP, Quantum Espresso, Abinit and Castep ...etc. due to its parallel efficiency. Moreover, according to Bloch's theorem, the wave function is already expressed as a combination of plane waves for a periodic system.

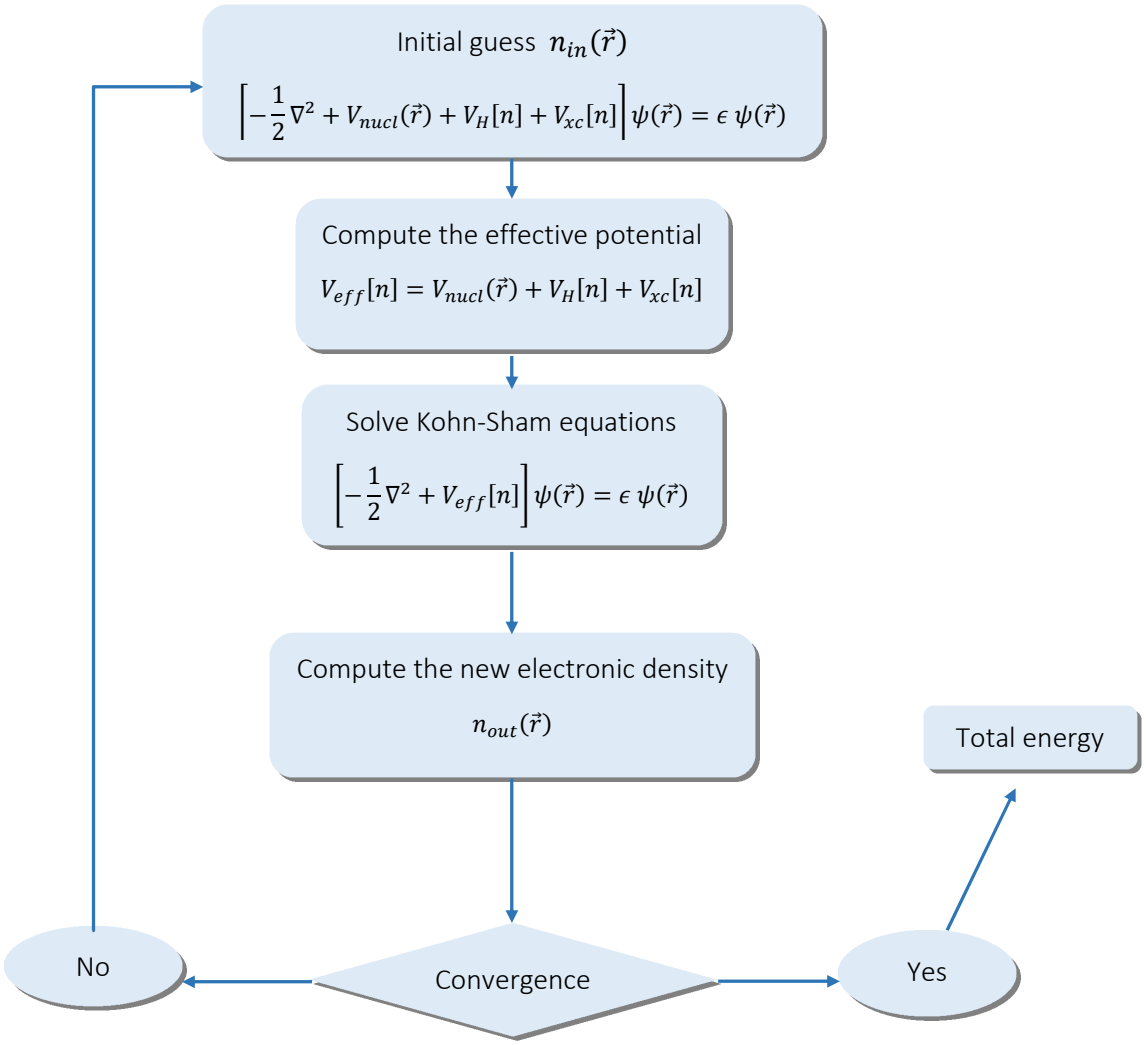

Figure 2.1: Iterative solution of KS equation.

2.3 Band structure

The band structure (BS) is a 2D representation of the allowed electronic energy levels in a crystalline material along specific high symmetry points in "k-space". BS gives many useful information on the studied material. It allow us to determine their nature e.g. metal, semimetal, insulating. Moreover, band dispersion directly reflect the carrier mobility, which will be explained in the next section.

2.3.1 Effective masses

According to the Eq 1.6 carrier mobility is directly, depend on the effective mass values. In this section, I will describe their concept and how we can compute their values using band

structure diagrams. As we previously said, many valuable information can be extracted from the band structure and their dispersion. In the band edge, the relationship between energy and wave vector could be modelled as free electron according to the following parabolic relation:

$$E(k) = \frac{h^2 k^{\mathbf{2}}}{2m_e} \tag{2.4}$$

So the effective mass is obtained by differentiating this relation

$$m_e = \frac{1}{h^2 \frac{d^2E(k)}{dk^2}} \tag{2.5}$$

From this relation a flatter band represents high effective mass while much more disperse band have lower effective mass. In order to compute the second derivative of energy with respect to the wave vector $\frac{d^2E(k)}{dk^2}$ with high accuracy we need a large number of points around energy band edge in the $E(k)$ curve.

2.3.2 Carrier mobility

High Electron-hole mobility (μ) is one of the most important characteristic for efficient absorber material. The experimental scheme is straightforward, but on the contrary, DFT computation is challenging. Indeed, to calculate carrier mobility we use deformation potential theory.[8, 9]. By applying low deformation along specific axe, it is possible to determine μ using following relation:

$$\mu = \frac{(8\pi)^{1/2} h^4 C_{ii}}{3E_l^2 m^{*5/2} (k_B T)^{3/2}} \tag{2.6}$$

Where $h, C_{ii}, E_l, m^*, k_B, and T$ are the reduced Planck constant, elastic constant, deformation potential constant, effective mass, Boltzmann constant, and temperature.

The elastic constants is calculated through the energy-strain curve by the following relation:

$$C_{ii} = \frac{1}{s_0} \frac{\partial^2 E}{\partial (l/l_0)^2} \tag{2.7}$$

Where E, l, l_0, and S_0 are the total energy, the lattice constant, the initial lattice constant and the unit cell's area respectively.

The deformation potential constant E_l is estimated using edge shift with respect to the strain

$$E_l = \frac{\partial E}{\partial l / l_0} \tag{2.8}$$

2.3.3 Band alignment

In multi-layer solar cells systems, the band position of absorber material should be aligned with partner layers [10, 11]. Indeed, the eigenvalues given by DFT periodic calculations have no significance because they depend on many calculation factors such as pseudo potential choice without any external energy reference. However, all materials have the same vacuum level, and therefore, we should determine valence band maximum (VBM) with respect to Vacuum level i.e. the ionization potential.

$$\mathrm{IP} = \mathrm{E_{vacuum}} - \mathrm{E_{VBM}} \tag{2.9}$$

A second calculation is required using slab model, we need big vacuum region in the order of 30 Å in order to avoid any interaction of the slab and its periodic image. Moreover, a large number of layers are required to assume that all layers in the middle behave as bulk as we present in Figure 2.2

The electrostatic potential should be the plateau in the empty space and their values represent the calculated vacuum level(see figure 2.3).

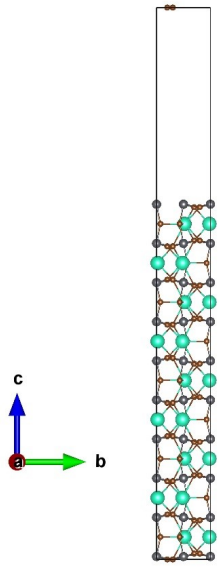

Figure 2.2: Slab model with large vacuum space.

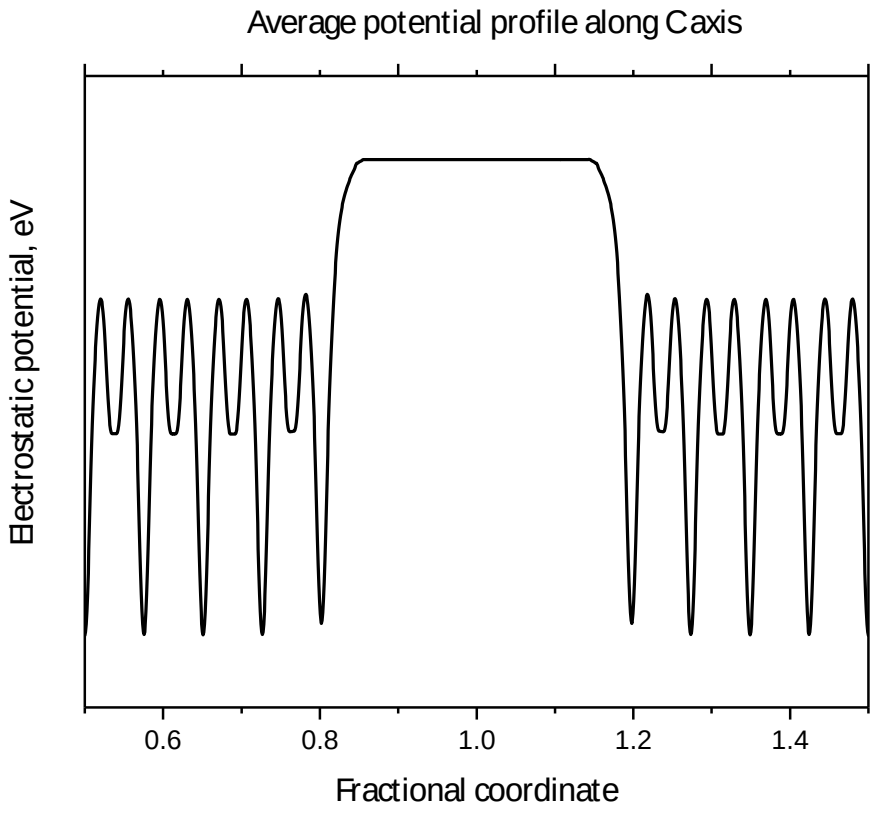

Figure 2.3: Electrostatic potential of slab model, the vacuum slab show a plateau in electrostatic potential for $CsPbI_3$.

The variation in the electrostatic potential is caused by different layers. In order to compute the IP we choose one core state and compare vacuum-core level in the slab calculation

with VBM-core level in the simple bulk calculation.

$$IP = (E_{vac} - E_{core,slab}) - (E_{VBM,bulk} - E_{core,\ bulk}) \tag{2.10}$$

2.4 Point defect

In all materials, point defects can be formed and are always present with different concentrations. They play important roles and dramatically influence material's properties and performances. They particularly modify mechanical, electronic, transport and optical behavior. Hence, the understanding of defects is crucial for wide range of technologies. Controlled presence of defects in a material allows the tuning of many useful properties for several applications such as optoelectronic devices, solar cells [12–16] , thermoelectricity [17–19], batteries [20–22] and catalysis... etc. Indeed, one of the most required characteristic for an efficient photovoltaic device (which is the main subject of this thesis) is the defect tolerance. This means that the intrinsic defects will not destroy the performance of solar cells by trapping the generated carriers. The semiconductor should be elaborated in special condition in order to reduce the SRH recombination rate. As consequence the generated carriers lifetime is long enough to be extracted [12, 13, 15]. Only defect chemistry could provide in depth understanding of the most required properties for battery materials such as theoretical capacity, cell voltage, transport and charge-transfer resistance... etc. [20–22]. Defects have also great influence on the behavior of electrons and phonons. It is possible to enhance power factor by tuning the carrier concentration and affect on the effective mass via the formation of resonant impurity levels. All these properties can be studied with much details that are very challenging to access through experimental way [23, 24]. In this section, we try to present the problem by giving a simple practical way and mention most recent toolkits that can be used to automate the treatment of point defects using DFT computation . For in depth understanding of the physics behind defect DFT computation and correction schemes, we highly recommend the much detailed review [23–29].

2.4.1 Defect types and notation

The most common point defects are vacancies (missing atoms), interstitials (self or impurities additional atoms incorporated on sites) and antisites. Point defects can be formed directly by removed, added or substituted atoms to a perfect structure.

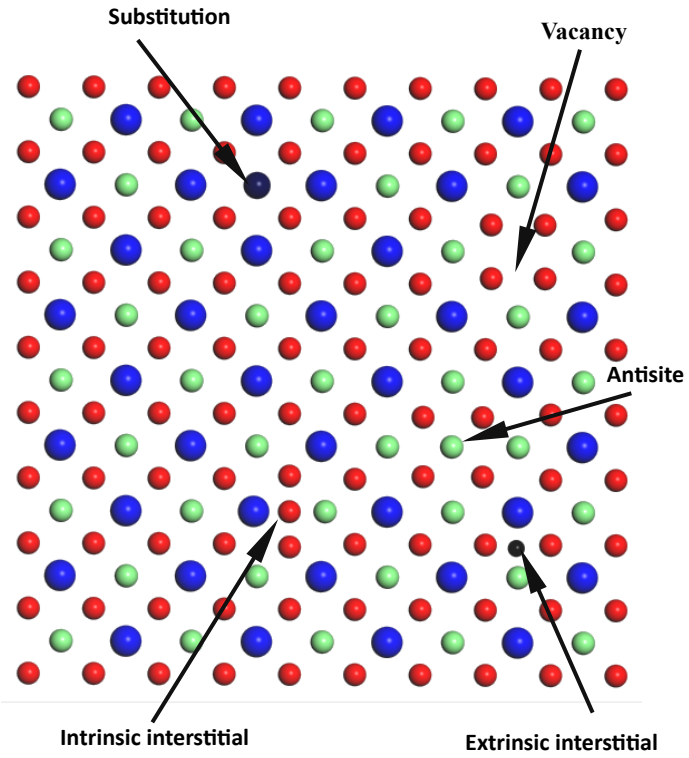

Figure 2.4: Different point defects top: substitution and vacancy, middle: antisites and bottom interstitial.

The challenge is how we identify the interstitial site most likely to be formed because of the large number of possibilities. Many methods were employed in order to find the most suitable tetrahedron, octahedron body-centered cubic, face-centered cubic and hexagonal close packed motifs environments. However the easiest and most effective method is provided in the python tools (Interstitial Finding Tool: InFiT) which was developed by Zimmermann et al [30].

Usually used notation relate defect types and species, for interstitial and vacancy can be represented by i and V respectively and define the type of atom i.e. Br_i (V_{Br}) for Bromine interstitial (vacancy), for substitution add X_Y notation where X is the new atomic species which occupy the atomic site of Y specie. For the charge we just add their numerical value, for example, the positively-charged Br-on-Cs is represented by Br_{Cs}^{+2}.

2.4.2 DFT simulation of point defect

DFT is a powerful tool that allows us to understand the behavior of defect in materials. Based on (relatively) simple formalism, it is possible to compute the defect formation energies by mean of first-principles ground-state calculations. We can also discuss the stability of different defects with different charge states. We are also able to calculate the deep and shallow thermodynamic transition levels and their concentration under various growth conditions. Point defects are simulated in a periodic system (periodic boundary conditions) using finite sized super cell Figure 2.5. It is well known that defect concentration is very low and defect-defect interactions are negligible. However, for small supercell the supposed concentrations are very high and defect interactions are present and affect calculated results. This issue will be dealt with in the coming sections.

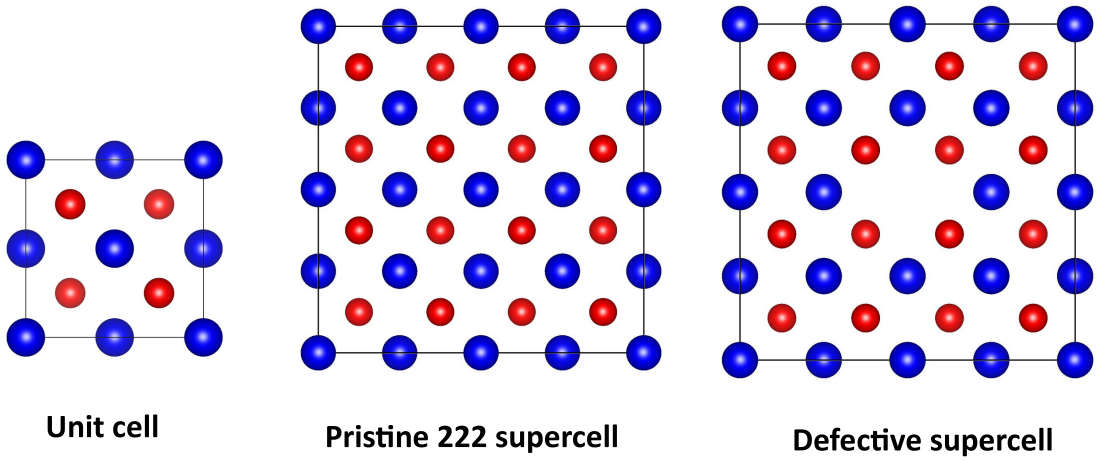

Figure 2.5: Supercell model to simulate point defect as a periodic system.

Other obstacle: we know about the DFT deficiency to predict the material's properties which are associated with the electronic structure especially the band gap, therefore, high performance strategy should be used such GW or hybrid calculation.

Based on DFT-SC simulation many important defect's properties can be calculated such as defect formation energy (DFE), ionisation level (IL) as well as defect concentration.

2.4.2.1 Defect formation energies (DFE)

DFE is the energy cost to create a defect X in a host material. The formation of a defect is governed by the Gibbs free energy $\Delta_f G = \Delta_f H - T\Delta_f S$. DFT calculation are carried out in the absence of temperature,and without any changes in volume or pressure, too.

$$\Delta_f G = \Delta_f H - T\Delta_f S \approx \Delta_f H = \Delta_f E + p\Delta V \approx \Delta_f E \tag{2.11}$$

$\Delta_f E$ is the total energy change that we can get through our DFT calculations. In general, simulated system can be divided into two categories: neutral and charged defect. For neutral defects, formation energy E_f is well converged according to SC size and can be calculated from the following Equation

$$E_f[X] = E_{\text{tot}}[X] - E_{\text{tot}}[\text{ bulk }] - \sum n_i \mu_i \tag{2.12}$$

$E_{\text{tot}}[X]$ is the total energy of the defective supercell, $E_{\text{tot}}[\text{ bulk }]$ is the total energy of the pristine bulk supercell (equivalent to defective one) and μ_i is the atomic chemical potentials of added ($n_i = +1$) or removed ($n_i = -1$) species from the pristine bulk supercell. On the other hand, for charged defect E_f converges particularly slowly while increasing supercell size. Due to interaction between defect images [23–29], correction term should be added (see Eq 2.13 and Figures 2.6 and 2.7). However, the correction magnitude could be sizeable.

$$E_f[X_q] = E_{\text{tot}}[X_q] - E_{\text{tot}}[\text{ bulk }] - \sum n_i \mu_i + qE_F + E_{\text{corr}} \tag{2.13}$$

$E_f[X]$ is similar to what we have just showed for the neutral defect and should be re-calculated by adding charge state q to the defect, while $E_{\text{tot}}[\text{ bulk }]$ and μ_i are exactly the same as neutral case. E_F is the Fermi level, qE_F is the electron chemical potential which is defined as the energy cost of adding or removing electrons and E_{corr} is the correction term.

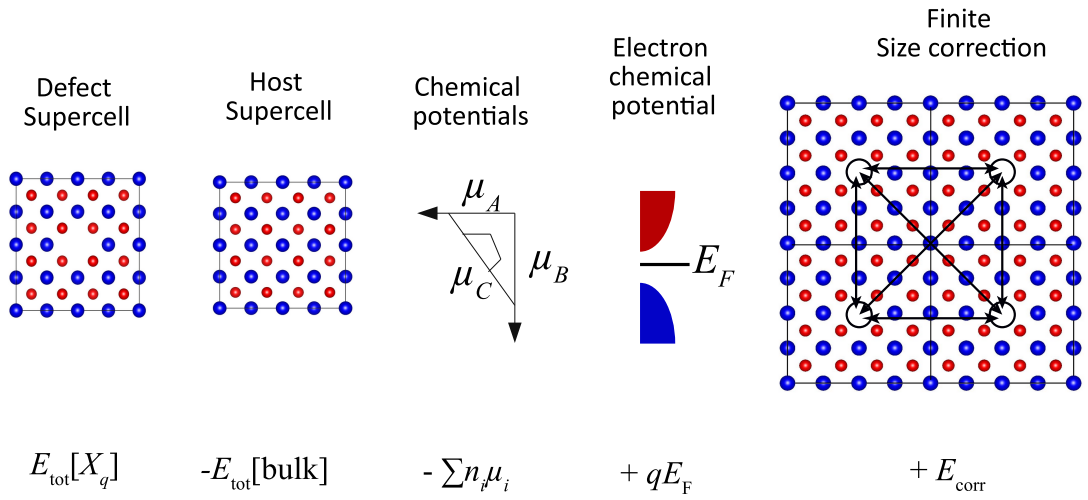

Figure 2.6: Defect formation energy calculation scheme through super cell model including corrections.

2.4.2.2 Chemical potentials

In thermodynamics, the change of particles number when a chemical species is added or removed makes change in the energy of studied system. Thermodynamic quantities could be written as follow:

$$\begin{aligned}
&\text{Free Gibbs energy} && dG = VdP - SdT + \sum \mu_i dn \\
&\text{Internal energy} && dU = -PdV + TdS + \sum \mu_i dn \\
&\text{Free energy} && dF = -PdV - SdT + \sum \mu_i dn \\
&\text{Enthalpy} && dH = VdP + TdS + \sum \mu_i dn
\end{aligned}$$

The chemical potential is defined as the change rate of free energy with respect to the change in the number of atoms:

$$\mu_i = \left(\frac{\partial U}{\partial n_i}\right)_{V,S} = \left(\frac{\partial F}{\partial n_i}\right)_{V,T} = \left(\frac{\partial H}{\partial n_i}\right)_{P,S} = \left(\frac{\partial G}{\partial n_i}\right)_{P,T} \tag{2.14}$$

Particles tend to move from higher to lower chemical potential. Based on this, the equilibrium conditions of chemical reaction and equilibrium phases are studied. Therefore, under different preparation (growth) conditions of the material, the atomic chemical potential can be defined. In general, μ_i is referenced to the total energy E_i of pure solid or molecule elements.

The change in total energy when we add or remove one electron is the electron chemical

potential which known as Fermi energy.

Chemical potential range can be computed using the following steps

1. Optimize all elements in their standard state (e.g. Br molecule and Cs pure bulk in $CsPbBr_3$), and compute the total energy.

2. Optimize other secondary phase (e.g. CsBr $PbBr_2$ for $CsPbBr_3$) and compute the total energy.

3. Optimize the host cell and compute the total energy.

4. Use all these boundaries to define chemical stability region and chose a representable point for Eq 2.13.

2.4.2.3 Correction terms

As discussed in previous sections, for charged defects and due to finite supercells we should add correction terms; first, for potential alignment due to the shift introduced by defect charge, the second corresponds to the electrostatic interactions between defects and their periodic images. Both terms are sizeable (i.e. decrease when use a larger SC Figure 2.7).

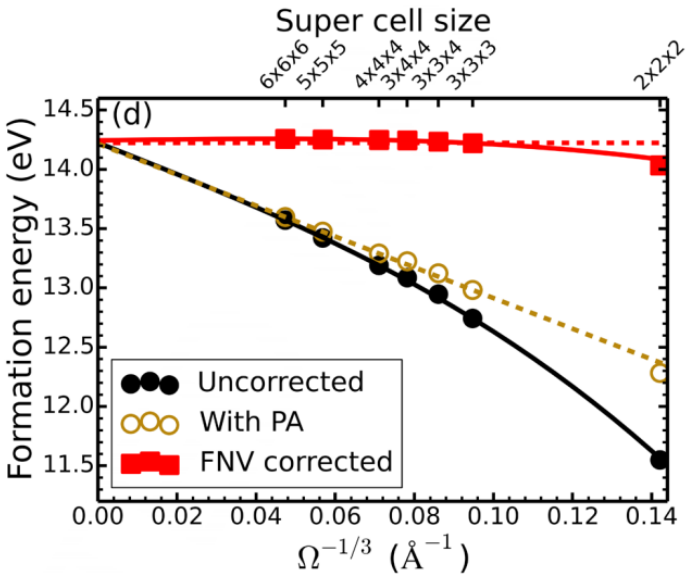

Figure 2.7: Convergence of formation energies with respect to super cell size for uncorrected formation energies, only potential alignment (PA), and Freysoldt-Neugebauer-Van de Walle (FNV) scheme. Reprinted from Ref [31] Copyright 2018 Elsevier B.V.

2.4.2.4 Potential alignment

Charged defect supercells and bulk supercells don't have the same reference for the electrostatic potential. However, all of the eigenvalues of defective supercell are shifted with respect to that of the pristine one. We must align the potentials using the following relation.

$$\Delta V_{el} = V_{\text{core},\,X} - V_{\text{core}\,,H} \tag{2.15}$$

Where $V_{\text{core},\,X}$ is the potential of one core level in the defective supercell and $V_{\text{core}\,,H}$ is the same core level in the host supercell.

2.4.2.5 Electrostatic correction

As discussed above, corrections are needed in order to take into account of the electrostatic interactions between charged defect sites and their periodic images. Many forms have been suggested for this correction, almost of them derived from the Madelung expression [32]:

$$E_{\text{Madelung}} = \frac{q^2\alpha}{2L} \tag{2.16}$$

where α is Madelung constant, and L the distances between the charges (point charges).

The charge density distribution around a defect is diffuse and doesn't correspond to point like model. Makov and Payne (MP) [33] treated charge screening in their expression by including the dielectric constant of the host structure as well as the interaction between charged defect quadrupolar moment of its charge density images. Charge is then treated as a localized charge distribution in vacuum.

$$\Delta E_{icc}^{MP} = \frac{q^2\alpha}{2\varepsilon L} - \frac{2\pi qQ}{3\varepsilon\Omega} \tag{2.17}$$

Where Q,and Ω are the quadrupole moment, and supercell volume.

Other schemes were proposed in order to simplify and enhance the electrostatic correction term such as:

• Lany and Zunger (LZ) in order to evaluate a second radial moment suggest the use of

the charge difference between both neutral and charged defect [27].

• Freysoldt, Neugebauer, and Van de Walle (FNV) suggested a new scheme with rapid convergence with cell size . In this scheme the correction energy is computed from pristine and defective supercell[25].

• Kumagai and Oba (KO) extended the FNV through the atomic site potentials and dielectric anisotropy [34].

2.4.2.6 Ionization levels

Point defects often create ionization levels (IL) (see Figure 2.8 and 2.9), which are also known as trap levels in the band gap or near the band edge where the defect can accept or donate electrons. Removing an electron/ hole from the trap conduction/valance band requires an energy which is relatively high for deep level.

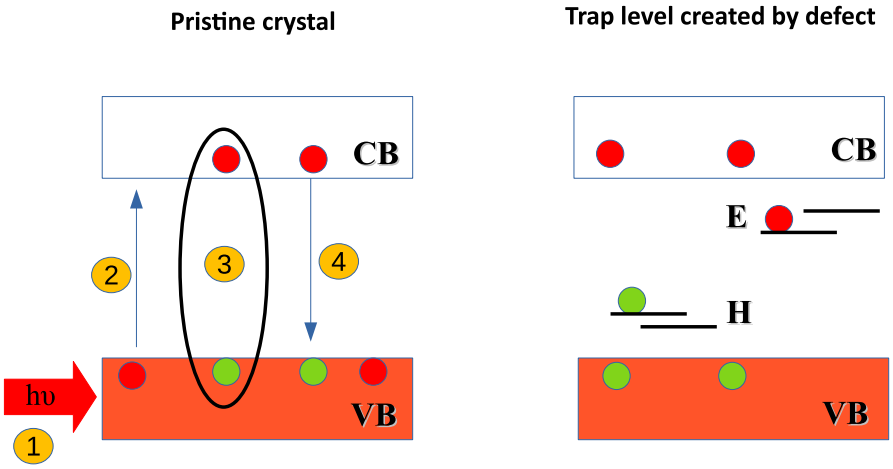

Figure 2.8: Carrier Generation and Recombination and defect effect. (1) sun-light (2) electron excitation (3) pair electron-hole (exciton) formation (4) recombination. Hole capture in H trap level and Electron capture E trap level created by defect..

According Eq 2.13 we plot DFE as a function of Fermi level position from VBM to CBM (see Figure 2.9). Neutral charge states appear as horizontal lines, while positive charge states increase from left to right, and negative charge states decrease. Transition level correspond to where the two charge states have the same energy in other words the intersection between two charge states.

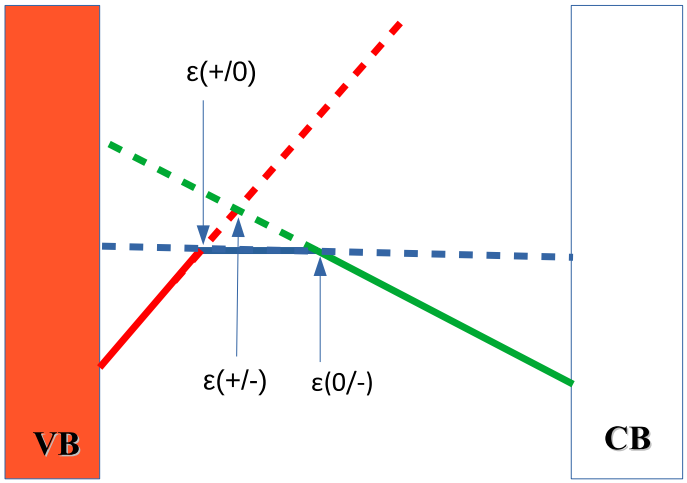

Figure 2.9: Schematic illustration of formation energy vs Fermi level for different charge state red, blue and green represent +1, 0 and -1 charge state respectively. Solid line indicate the most energetically charge state. Three transition deep level were presented

2.4.2.7 Practical way

Recently, many softwares have been developed with useful interface to automat DFT simulation of point defect, which read potential file in cube/xsf format that can be provided by many DFT codes. In Table 2.1 we summarize their correction schemes, compatible ab initio code and a short description.

Table 2.1: List of widely used toolkit for defect study with a short description and compatible DFT code.

Software	Description
PyCDT Python Charge Defects Toolkit[35]	Python package can be used to generate input files required for DFT calculation and process the result to directly compute DFE, IL. Build initially for vasp
PyDEF [36]	post-treatment software for ab-initio simulation with simple Graphical User Interface (GUI). Build initially for vasp
CoFFEE [31]	Python toolkit to process DFT result. Tested for wide range of material bulk, slab (or two-dimensional), wires and nanoribbons. Quantum Espresso was used as test in their paper but can be used with vasp code.
Pylada-defects [37]	A computational framework to automate point defect calculations through VASP code.
Sxdefectalign [25, 26]	A simple toolkit for defect energy correction computation directly read potential file provided by different ab initio codes, created for SPHInX and now can be used for VASP, Socorro and quantum espresso codes. Already included in PyCDT

We note that the most used correction scheme for all toolkits is FNV due to its improved results in numerous materials.

2.4.3 Summary

In general, DFT simulation of point defect can be summarized as follow: first generate point defect, perform optimization and calculate DFE and other related properties.

1. Generate defective structure

   • Vacancy, antisite, substitution and use a software like InFiT for interstitial defect generation.

2. Perform DFT calculation

   • Pristine structure geometry optimization, dielectric constant and generate potential file.

   • Defective structure (only relaxation) compute total energy and generate potential files.

   • Pure atom and molecule full optimisation.

3. Collection of parameter

- Total energies to plot chemical potential range.
- Compute potential shifting and electrostatic correction.

4. Analysis
   - Compute the DFE.
   - Compute IL.

Refrences

[1] Born, M. and Oppenheimer, R., *Annalen der physik*, 1927, **389**(20), 457–484.

[2] Hohenberg, P. and Kohn, W., November , (1964), **136**(3B), B864–B871.

[3] Kohn, W. and Sham, L. J., November , (1965), **140**(4A), A1133–A1138.

[4] Ceperley, D. M. and Alder, B. J., August , (1980), **45**(7), 566–569.

[5] Perdew, J. P.; Burke, K. and Ernzerhof, M., October , (1996), **77**(18), 3865–3868.

[6] Perdew, J. P.; Burke, K. and Ernzerhof, M., February , (1997), **78**(7), 1396–1396.

[7] Heyd, J.; Scuseria, G. E. and Ernzerhof, M., June , (2006), **124**(21), 219906.

[8] Wei, S.-H.; Zunger, A. and Franceschetti, A., December , (1994), **50**(24), 17797–17801.

[9] Shockley, W. and Bardeen, J., October , (1950), **80**(1), 72–80.

[10] Wei, S.-H. and Zunger, A., July , (1987), **59**(1), 144–147.

[11] Wei, S.-H. and Zunger, A. In *Electronic Structure of Semiconductor Heterojunctions*, Margaritondo, G., Ed., Perspectives in Condensed Matter Physics; Springer Netherlands, Dordrecht, 1988; pages 200–203.

[12] Kang, J. and Wang, L.-W., January , (2017), **8**(2), 489–493.

[13] Meggiolaro, D.; Motti, S. G.; Mosconi, E.; Barker, A. J.; Ball, J.; Perini, C. A. R.; Deschler, F.; Petrozza, A. and Angelis, F. D., March , (2018), **11**(3), 702–713.

[14] deQuilettes, D. W.; Vorpahl, S. M.; Stranks, S. D.; Nagaoka, H.; Eperon, G. E.; Ziffer, M. E.; Snaith, H. J. and Ginger, D. S., May , (2015), **348**(6235), 683–686.

[15] Leijtens, T.; Eperon, G. E.; Barker, A. J.; Grancini, G.; Zhang, W.; Ball, J. M.; Kandada, A. R. S.; Snaith, H. J. and Petrozza, A., November , (2016), **9**(11), 3472–3481.

[16] Chen, Y.; Yi, H. T.; Wu, X.; Haroldson, R.; Gartstein, Y. N.; Rodionov, Y. I.; Tikhonov, K. S.; Zakhidov, A.; Zhu, X.-Y. and Podzorov, V., August , (2016), **7**(1), 12253.

[17] Levander, A. X.; Tong, T.; Yu, K. M.; Suh, J.; Fu, D.; Zhang, R.; Lu, H.; Schaff, W. J.; Dubon, O.; Walukiewicz, W.; Cahill, D. G. and Wu, J., *Appl. Phys. Lett.*, 2014, page 4.

[18] Karthikeyan, V.; Li, T.; Medasani, B.; Luo, C.; Shi, D.; Wong, J. C. K.; Lam, K.-H.; Ling, F. C. C. and Roy, V. A. L., *Advanced Electronic Materials*, 2020, **6**(4), 1901284.

[19] Pei, Y.; Zheng, L.; Li, W.; Lin, S.; Chen, Z.; Wang, Y.; Xu, X.; Yu, H.; Chen, Y. and Ge, B., 2016, page 8.

[20] Maier, J., *Journal of The Electrochemical Society*, 2015, page 7.

[21] Pan, Y., *Journal of Alloys and Compounds*, 2019, page 6.

[22] Edelberg, D.; Rhodes, D.; Kerelsky, A.; Kim, B.; Wang, J.; Zangiabadi, A.; Kim, C.; Abhinandan, A.; Ardelean, J.; Scully, M.; Scullion, D.; Embon, L.; Zu, R.; Santos, E. J. G.; Balicas, L.; Marianetti, C.; Barmak, K.; Zhu, X.; Hone, J. and Pasupathy, A. N., *Nano Lett.*, 2019, page 9.

[23] Freysoldt, C.; Grabowski, B.; Hickel, T.; Neugebauer, J.; Kresse, G.; Janotti, A. and Van de Walle, C. G., March , (2014), **86**(1), 253–305.

[24] Seebauer, E. G. and Kratzer, M. C., December , (2006), **55**(3), 57–149.

[25] Freysoldt, C.; Neugebauer, J. and Van de Walle, C. G., January , (2009), **102**(1), 016402.

[26] Freysoldt, C.; Neugebauer, J. and Walle, C. G. V. d., *physica status solidi (b)*, 2011, **248**(5), 1067–1076.

[27] Lany, S. and Zunger, A., November , (2009), **17**(8), 084002.

[28] Castleton, C. W. M.; Höglund, A. and Mirbt, S., November , (2009), **17**(8), 084003.

[29] Van de Walle, C. G. and Neugebauer, J., March , (2004), **95**(8), 3851–3879.

[30] Zimmermann, N. E. R.; Horton, M. K.; Jain, A. and Haranczyk, M., *Frontiers in Materials*, 2017, **4**.

[31] Naik, M. H. and Jain, M., May , (2018), **226**, 114–126.

[32] Leslie, M. and Gillan, N. J., February , (1985), **18**(5), 973–982.

[33] Makov, G. and Payne, M. C., February , (1995), **51**(7), 4014–4022.

[34] Kumagai, Y. and Oba, F., May , (2014), **89**(19), 195205.

[35] Broberg, D.; Medasani, B.; Zimmermann, N. E.; Yu, G.; Canning, A.; Haranczyk, M.; Asta, M. and Hautier, G., May , (2018), **226**, 165–179.

[36] Péan, E.; Vidal, J.; Jobic, S. and Latouche, C., March , (2017), **671**, 124–130.

[37] Goyal, A.; Gorai, P.; Peng, H.; Lany, S. and Stevanovic, V., April , (2017), **130**, 1–9.

3

Lead iodide perovskite polymorphs $CsPbI_3$

In this chapter, we use PP-PW method to investigate structure stability, electronic and optical properties as well as some carrier transport parameters of $CsPbI_3$ perovskites polymorphs, which according to last finding could replace $MAPbI_3$ for more stable perovskite solar cells with high power conversion efficiency. This chapter is a modified version of our paper [1] entitled "First-principles investigation on the stability and material properties of all-inorganic cesium lead iodide perovskites $CsPbI_3$ polymorphs" published in PhysicaB: Condensed Matter and has been reproduced here with the permission of the copyright holder.

3.1 Introduction

Perovskite solar cells (PSCs) have attracted much attention in recent years. Compared to other conventional solar cell materials, they provide the lowest production cost in solar energy technology [2–6] with high power conversion efficiencies (PCE) approaching 24% [7]. In just few years following their discovery, these materials outperformed Cadmium Telluride (CdTe) and not far from high-purity and high production cost crystalline silicon solar cell 26% [8]. However, organometallic perovskite are unstable and very sensitive to moisture and oxygen due to the present of organic cations MA and FA. Indeed, the smaller cation Cs+ (1.67 Å) has been used to replace organic cation MA+ (1.80 Å) or FA+ (1.90 Å) which resulted in a higher thermal stability [9–15] and high PCE of 13.4% for quantum dot devices [11] and 15.1 % for a thin films [10]. $CsPbI_3$ has many phases. Cubic perovskite (Pm3m) is the most studied among $CsPbI_3$ perovskites [16–19] with Eg =1.73 eV [14], which is almost ideally suited for perovskite-silicon tandem solar cell [12]. Many works have reported that this phase can be stabilized only at temperatures above 300 °C [12, 20]. M. Roknuzzaman et al. [21] reported theoretical investigation of structural, electronic, mechanical and optical properties of Pb and lead-free inorganic metal halide cubic perovskites and showed that these compounds are mechanically stable and have low reflectivity and high optical absorption coefficients with suitable direct gap. More recently, R. J. Sutton et al. [9], have prepared orthorhombic (SG Pnam) black $CsPbI_3$ thin-films, using high and low-temperature preparation routes. By means of ab initio electronic structure calculations, they also investigated the band structure of Pnam phase and showed that this phase is energetically the most stable polymorph among $CsPbI_3$ perovskites.

The fundamental properties of perovskite absorber materials are largely unknown, a good understanding of the structure effect on the different physical properties of $CsPbI_3$ perovskite polymorphs, especially octahedral tilting impact is required [22]. In this chapter, we report a theoretical study on the $CsPbI_3$ perovskite polymorphs using density functional theory. We investigate the structural, electronic, optical, and some carrier transport properties of cubic, tetragonal and orthorhombic black phases.

3.2 Computational detail

The pseudopotential plane-wave(PP-PW) method as implemented in Cambridge Sequential Total Energy Package (CASTEP) module of material studio [23, 24] was used. The electron-ion potential is described in average by norm-conserving Pseudopotentials [25]. Different exchange and correlation functionals are used namely Local density approximation (LDA) [26], Perdew–Burke–Ernzerhof generalized gradient approximation(GGA-PBE) [27] and PBE for surface and solid (PBEsol) [28]. Pseudo atomic calculation were performed for Cs:$5s^2\ 5p^6\ 6s^1$, Pb:$5s^2\ 5p^6\ 5d^{10}\ 6s^2\ 6p^2$ and I:$5s^2\ 5p^5$.

The plane-wave cutoff energy of 600 eV was used throughout our investigations. For crystal structure relaxation, we choose k-point mesh of (6×6×6), (4×4×5) and (4×4×3) for the cubic tetragonal and orthorhombic phases respectively. Using Broydene-Fletchere-Goldarbe-Shanno (BFGS) method [29], all atomic general positions were relaxed until the atomic forces were less than 0.01 eV/Å with maximum stress 0.02 GPa. For the electronic and optical properties, we used a denser k-point mesh of (8×8×8), (6×6×8) and (6×6×4) for the cubic tetragonal and orthorhombic phases respectively. For better calculations of the electronic properties, especially to determine more precise band gap, non-local hybrid exchange-correlation functional (HSE06) [30] has been used.

3.3 Structure and material stability

Cesium lead iodide $CsPbI_3$ has many phases; active black phases synthesised at high temperature having space groups Pm-3m, P4/mbm and Pnam phases for which the unit cells contain 5,10 and 20 atoms respectively, and inactive yellow phase (Pnma) at low temperature. The challenge now is how to form the black phase at room temperature [9, 12, 13]. Indeed, cubic phase is formed at 360 ^{0}C upon cooling, however, tetragonal and orthorhombic black phases are formed at 260 ^{0}C and 175 ^{0}C respectively. Examination of their crystal structures revels that these polymorphs differ mainly in PbI_6 octahedra, (see Figure 3.1).

First step for ab initio method is the optimization of targeted structures by the minimization of internal forces and pressure. For the α-phase (Pm3m) and γ-phase (Pnam) we

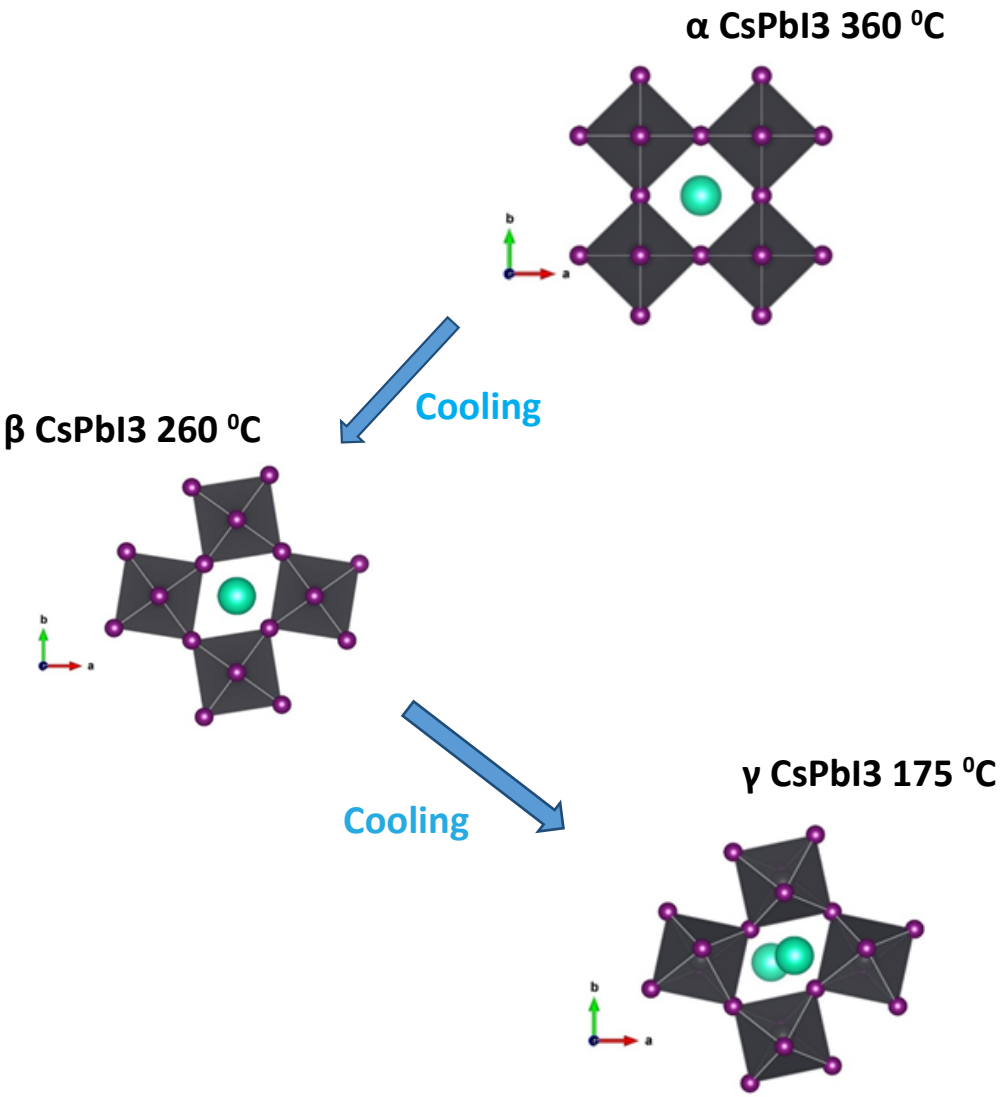

Figure 3.1: Ideal perovskite α(Cubic) phase and lower-symmetry β(tetragonal) and γ(orthorhombic) phases

start from the experimental crystal structures given by R. J. Sutton et al [9]. The β-phase (P4/mbm) is isostructural to $CsSnI_3$ hence, we use the latter structure as a starting point. The functional choice is of great importance to treat solid system. It is well known that LDA(GGA-PBE) always lower(higher) estimate lattice parameter and therefore we used also PBEsol for better description of the ground state properties. The calculated lattice constants are summarized in Table 3.1. Our calculated results are in good agreement with experimental values [9, 31] especially those obtained using PBEsol for α (γ) phases with disagreement of the order of 0.2% a (1.02% a, 0.35% b and 0.56 % c).

Furthermore, we evaluate the thermodynamic stabilities of $CsPbI_3$ phases by calculat-

ing formation energies of our compounds from CsI and PbI_2 precursors using the following relation:

$$\Delta H_f \approx \Delta E_f = E\left[CsPbI_3\right] - E\left[CsI\right] - E\left[PbI_2\right] \tag{3.1}$$

Table 3.1: Summary of calculated structural parameters and formation energies for $CsPbI_3$ perovskites polymorphs compared to available theoretical and experimental data.

			Lattice parameter (Ångström)	Formation energy (eV)
				CsI+PbI_2
α-$CsPbI_3$	This work	LDA	a= 6.15	0.075
		PBE	a= 6.41	0.010
		PBEsol	a= 6.27	0.047
	other		a= 6.289 [c] 6.26 [d] 6.39 [e]	
β-$CsPbI_3$	This work	LDA	a= 8.44 c= 6.28	-0.074
		PBE	a=8.86 c= 6.51	-0.074
		PBEsol	a=8.67 c= 6.37	-0.051
	other	***		
γ-$CsPbI_3$	This work	LDA	a= 8.95 b= 7.99 c= 12.17	-0.149
		PBE	a= 9.12 b= 8.79 c =12.67	-0.107
		PBEsol	a =8.95 b= 8.55 c= 12.40	-0.091
	other		[b] a = 8.86 b = 8.58 c = 12.47	

a exp α $CsPbI_3$ 634 K [31]
b exp γ $CsPbI_3$ [9]
c PBEsol [18]
d PBE [19]
e FP-LAPW GGA [16]

We can see clearly that the cubic phase has positive formation energy and therefore, this phase is energetically unstable. The orthorhombic γ-phase is the most stable with total energy lower by 9.9 meV and 13.9 meV (PBEsol) per unit formula than tetragonal and cubic phases respectively. In general, this result agrees with previous work[9].

We should note here that, for good comparison between total energies of $CsPbI_3$ phases, we used the same calculation parameters (sampling 0.03 A^{-1} and Ecut 600 eV). From this point on, we are only interested in stable structures.

3.3.1 Thermodynamic stability regions

The equilibrium conditions of chemical reaction and equilibrium phases can be evaluated by studying different possible species in chemical reaction (for more information see chapter 2). Chemical potential range can be computed using the following conditions:

$$\mu_{Cs} + \mu_{Pb} + 3\mu_I = \Delta H \left(-5.88 \text{ for } \gamma - CsPbI_3 \text{ and } -5.84 \text{ for } \beta - CsPbI_3\right) \tag{3.2}$$

To avoid the formation of CsI and PbI_2 secondary phases, we must apply the following limits:

$$\mu_{Cs} + \mu_I < \Delta H(CsI) = -3.39\text{eV} \tag{3.3}$$

$$\mu_{Pb} + 2\mu_l < \Delta H(PbI2) = -2.40\text{eV} \tag{3.4}$$

Thus

$$\mu_{Pb} + 2\mu_I > -2.49 \text{ for } \gamma\text{CsPbI}_3 \text{ and } -2.46 \text{ for } \beta\text{CsPbI}_3 \tag{3.5}$$

Now we can plot the thermodynamic stability regions

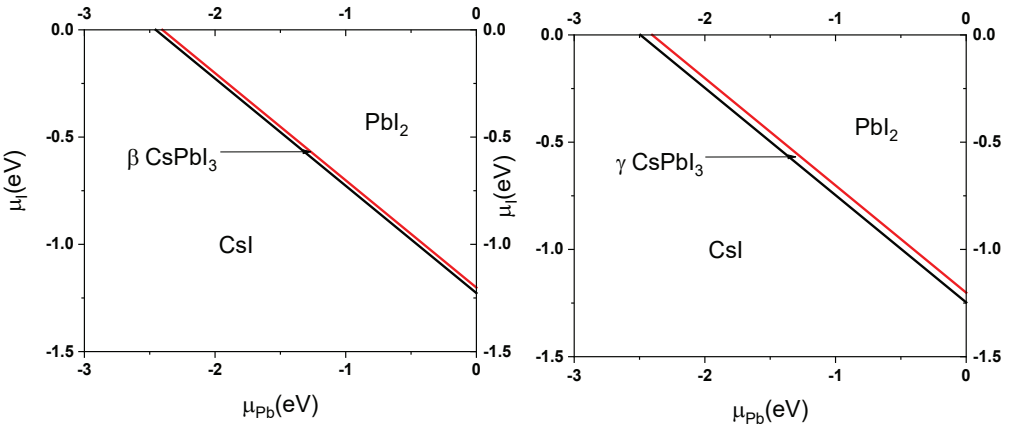

Figure 3.2: Stability diagram of $\gamma - CsPbI_3$, $\beta - CsPbI_3$, CsI and PbI_2 compounds obtained by PBEsol calculations

It is clear that the stability region is narrower in $\beta - CsPbI_3$ compared to $\gamma - CsPbI_3$ phase, a smaller energy is therefore needed to decompose $CsPbI_3$ into CsI and PbI_2.

3.4 Electronic properties

3.4.1 Band structure

Experimentally, $CsPbI_3$ perovskites have band gaps values around 1.7 eV and according to our calculations, all three structures are characterized by a direct band gaps as shown in Figure 3.3. The band gap of cubic phase is located at the R point in the Brillouin zone. However, the cubic to tetragonal to orthorhombic transitions folds the band edges from R-to-Z-to-G (see Figure.3.3).

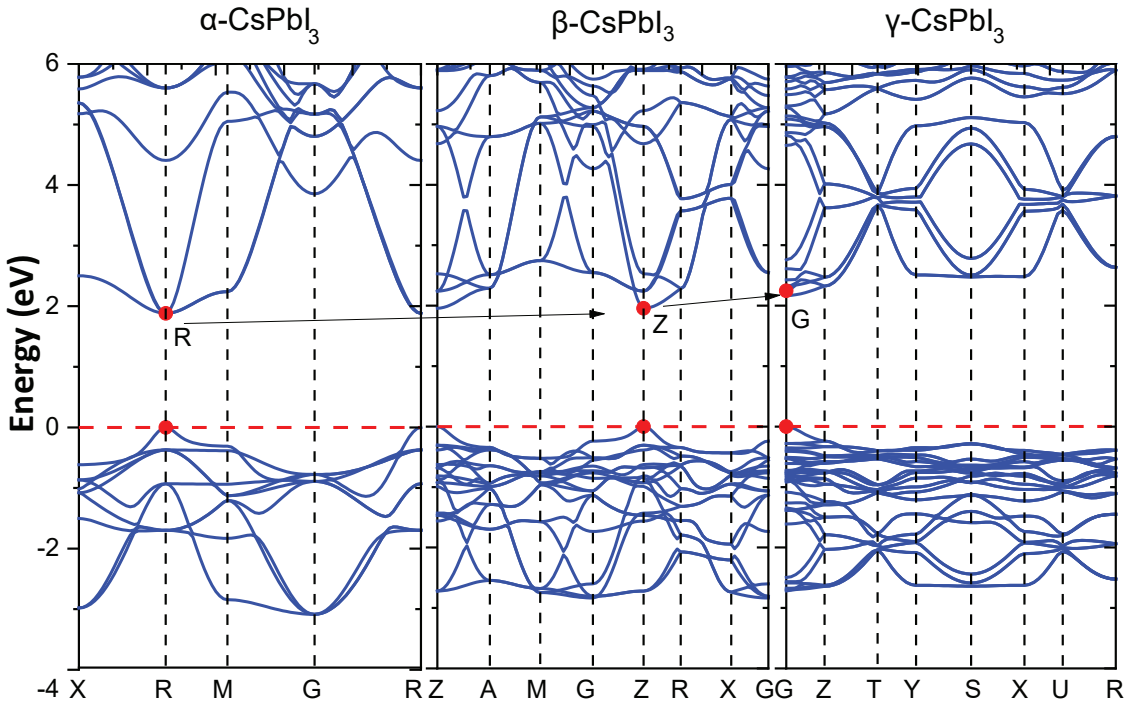

Figure 3.3: Calculated electronic energy band structures along the principal high-symmetry directions in the Brillouin zone for $CsPbI_3$ perovskites using the GGA-PBE functional.

We computed the Kohn-Sham(KS) band structures of $CsPbI_3$ perovskites. We know the band dispersion calculated using this method is reasonable but the calculated band gap energy is quantitatively wrong. In order to compute Eg much more accurately we used the hybrid functional HSE06. Many theoretical works[32–36] verified the important role of the spin orbit coplling (SOC) effect especially for heavy elements (lead atom in our case). In order to check the importance rule of the relativistic effect of the heavy metallic elements we calculated the electronic band structures with and without the SOC, which

split and downshift of the degenerated unoccupied Pb^{+2} p orbitals. Table 3.2 summaries, the results of band gap calculations, with and without SOC, for $CsPbI_3$ perovskites. For comparison, results of previous works are also included in table 3.2. It should be noted that the calculated band gaps without SOC effects are in much good agreement with slight overestimation (underestimation) compared to the experimental value of 1.73 eV using PBE(PBEsol). This is due to the fortuitous error cancellation between overestimation when ignoring the SOC effect and the well-known DFT underestimation error. Therefore, when we include the SOC, the underestimations of the band gaps become around 1.1 eV for both β and γ phases due to the well-known DFT deficiency and limitations.

Table 3.2: Calculated band gaps (eV) for $CsPbI_3$ perovskites with and without SOC.

		γ-$CsPbI_3$	β-$CsPbI_3$
This work	GGA-PBE (withSOC)	1.78(0.68)	1.598(0.54)
	PBEsol (withSOC)	1.517(0.59)	1.271(0.46)
	HSE06	2.01	1.9
Other work		1.2* 1.57** 1.72***	
* LDA,** GW and ***exp.[9]			

3.4.1.1 Density of state

For good understanding of the electronic properties, we computed the density of states (DOS). Figure 3.4 shows that the calculated DOS of our three phases present many similarities.

The Cs s and p states are far from the band edges, which are mainly formed by Pb and I states. The conduction band minimum (CBM) is the result of Pb 6p states contributions (weakly bonding with I 5p orbitals) while the valence band maximum (VBM) is mainly formed by contribution of Pb 6s and I 5p anti-bonding hybridized states. Indeed, the electronic transition from Pb s to Pb p states and I p to Pb p states have high probabilities which indicates Pb atoms impact on electronic and optical properties of $CsPbI_3$ perovskites.

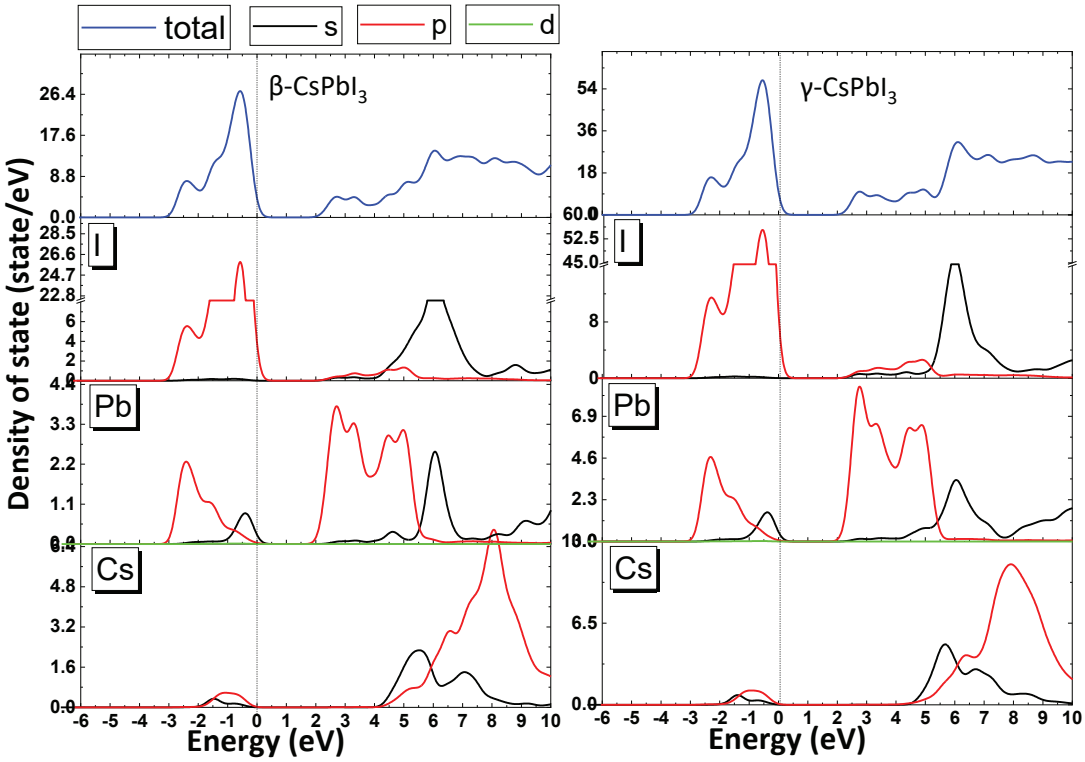

Figure 3.4: Calculated electronic density of state of cesium lead halide perovskites (β and δ phases).

3.4.2 Optical properties

3.4.2.1 Dielectric function

The response of a solid to the perturbation of an external electric field is described by the complex dielectric function $\tilde{\varepsilon}(\omega) = \varepsilon_1(\omega) + \varepsilon_2(\omega)$). The imaginary part determines the possibility of all (inter band) electronic direct transitions for a photon energy value. It is calculated from the momentum matrix elements between the occupied and unoccupied electronic states given by:

$$\varepsilon_2 = \frac{2e^2\pi}{\Omega\varepsilon_0} \sum_{k,v,c} |\langle \psi_k^c | \vec{u}\vec{r} | \psi_k^v \rangle|^2 \, \delta\left(E_k^c - E_k^v - E\right) \tag{3.6}$$

Where $\vec{u}$ is the vector defining the polarization of the incident electric field and $\psi_k^c \psi_k^v$ represent the valence and the conduction band states in which the direct transitions are possible.

On the other hand, the real part ε_1, directly related to the refractive properties, and it is

determined by Kramers-Kronig relation which takes the form

$$\varepsilon_1 = 1 + \frac{2}{\pi}\int_0^{\infty} \frac{\omega' \varepsilon_2(\omega\prime)}{\omega'^2 - \omega^2} d\omega' \tag{3.7}$$

Figure 3.5 shows the calculated dielectric function $\varepsilon(\omega)$ in the energy range from 0 up to 15 eV for $CsPbI_3$ perovskites.

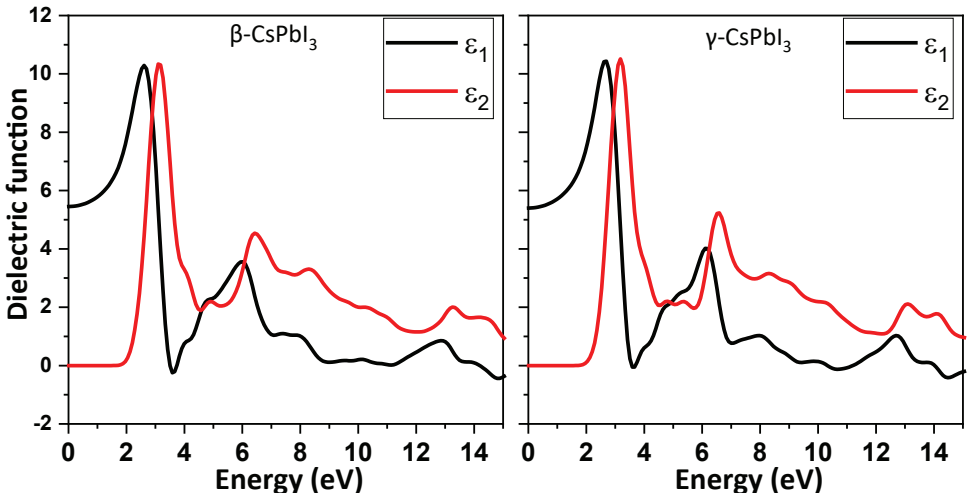

Figure 3.5: Frequency dependent dielectric function for $CsPbI_3$ perovskites polymorphs. Calculated within GGA.

The electronic vertical inter-band transitions from the valence to the conduction band described by the variations of the imaginary part $\varepsilon_2(\omega)$ (red lines) a dominant peak at 3.03 eV. This peak corresponds to the transitions from I p and Pb s states to p state of Pb atom.

3.4.2.2 Optical Absorption

The absorption coefficient α is computed from the ε_1 and ε_2 via the following relation:

$$\alpha(\omega) = \frac{2\omega}{c}\sqrt{\frac{\sqrt{\varepsilon_1^2(\omega) + \varepsilon_2^2(\omega)} - \varepsilon_1}{2}} \tag{3.8}$$

Figure 3.6 shows the calculated optical absorption of $CsPbI_3$ perovskites. This figure reveals that $CsPbI_3$ perovskites are characterized by high absorption coefficient values ($\alpha = 10^4 to 10^5 cm^{-1}$) due to the high values of DOS and direct band gap. These values are greater than absorption coefficient of conventional materials such as CdTe as depicted

in Figure 3.6.

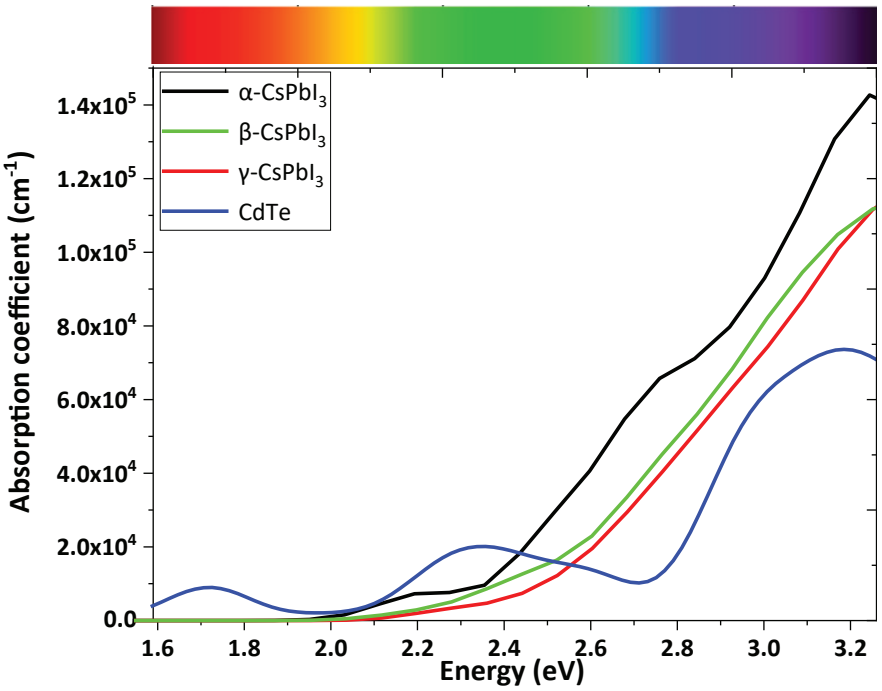

Figure 3.6: Photo-absorption coefficients of cesium lead halide perovskites polymorphs (α, β and γ phases) with CdTe coefficient for comparison calculated within GGA.

In general, all studied phases have the same optical characteristics with short increase of absorption for lower-symmetry tetragonal and orthorhombic perovskites. The ideal perovskite structure, however, has the best optical characteristic in accordance with previous results.

3.4.3 Carrier transport properties

In order to study the behavior of photo generated electrons and holes after photon absorption we calculate their effective masses and exciton binding energies. The effective masses were calculated at the Brillouin points Z and G for both energetically stable $\beta(\gamma)$ phases using refined energy band structure (0.001 Å^{-1} separation between consecutive k-points on the reciprocal space path) within the parabolic approximation.

Table 3.3 presents the calculated electron, hole and reduced effective masses and exciton binding energies E_b^{ex} for both β and γ $CsPbI_3$ perovskites.

We find that the reduced effective masse of γ-$CsPbI_3$ calculated within SOC+GGA

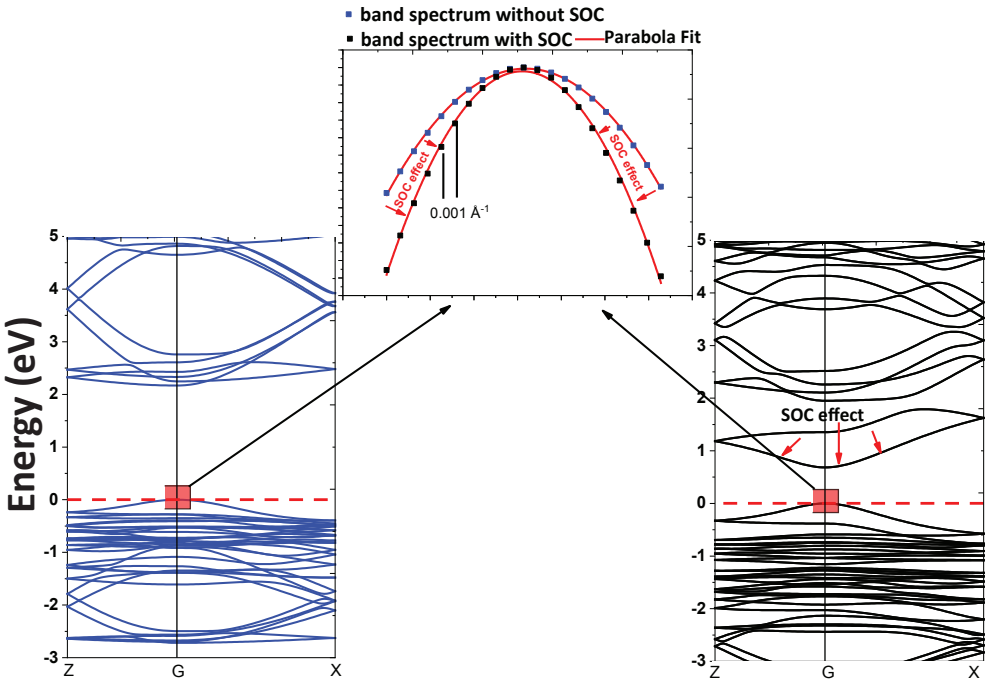

Figure 3.7: Refined band edge plot and SOC effect for hole effective mass calculation for δ-$CsPbI_3$ perovskite using parabolic fitting.

Table 3.3: Calculated effective masses and exciton binding energy for β and γ $CsPbI_3$ perovskites within GGA without (with SOC). Masses are given in units of the free electron mass m_0.

	m_h	m_e	μ	ε_s	E_b^{ex} (eV)
β-$CsPbI_3$	0.29(0.11)	0.32(0.14)	0.15(0.06)	5.46	0.068
γ-$CsPbI_3$	0.28(0.17) 0.23[a]	0.34(0.20),0.24[a]	0.15(0.09),0.114[b],0.12[a]	5.40	0.070
a GW [9]					
b exp [37]					

are in good agreement with experimental data with slight underestimations. Furthermore, the SOC also has an important effect on the effective masses. When SOC is included in the calculations, the effective masses are underestimated and become 0.11(0.14) and 0.17(0.20)for $m_e^*(m_h^*)$ of β-$CsPbI_3$ and γ-$CsPbI_3$ respectively. By comparison, the electron and hole effective masses within GW [9] are in excellent agreement with slight overestimation compared to experimental values. The exciton binding energies were calculated within the weak Mott-Wannier model, using the following relation[38]:

$$E_b^{ex} = 13.56\frac{\mu}{\varepsilon_s^2} \tag{3.9}$$

Where μ is the reduced effective mass $\left(\frac{1}{\mu} = \frac{1}{m_e^*} + \frac{1}{m_h^*}\right)$ and ε_s is the static dielectric constant.

All studied $CsPbI_3$ perovskites show low exciton binding energy light charge carriers, which makes them efficient absorbing materials.

3.4.4 Conclusion

In summary, using DFT and PP-PW method, we have systematically investigated the structural, electronic and optical properties of the cesium lead iodide perovskites polymorphs. Our results demonstrate that the orthorhombic Pnam phase is the most stable one. In addition, from the density of states we identified the important contribution of Lead atom to the electronic and optical properties, which have direct influence on light absorption of these materials. Our results show that these compounds have low effective masses and low exciton binding energies leading to high absorption coefficient values ($\alpha = 10^4 - 10^5 cm^{-1}$).

Refrences

[1] Fadla, M. A.; Bentria, B.; Dahame, T. and Benghia, A., May , (2020), **585**, 412118.

[2] Kojima, A.; Teshima, K.; Shirai, Y. and Miyasaka, T., May , (2009), **131**(17), 6050–6051.

[3] Lee, M. M.; Teuscher, J.; Miyasaka, T.; Murakami, T. N. and Snaith, H. J., November , (2012), **338**(6107), 643–647.

[4] Kim, H.-S.; Lee, C.-R.; Im, J.-H.; Lee, K.-B.; Moehl, T.; Marchioro, A.; Moon, S.-J.; Humphry-Baker, R.; Yum, J.-H.; Moser, J. E.; Grätzel, M. and Park, N.-G., August , (2012), **2**.

[5] Snaith, H. J., November , (2013), **4**(21), 3623–3630.

[6] Katan, C.; Mercier, N. and Even, J., March , (2019), **119**(5), 3140–3192.

[7] Jeon, N. J.; Na, H.; Jung, E. H.; Yang, T.-Y.; Lee, Y. G.; Kim, G.; Shin, H.-W.; Il Seok, S.; Lee, J. and Seo, J., August , (2018), **3**(8), 682–689.

[8] Yoshikawa, K.; Kawasaki, H.; Yoshida, W.; Irie, T.; Konishi, K.; Nakano, K.; Uto, T.; Adachi, D.; Kanematsu, M.; Uzu, H. and Yamamoto, K., May , (2017), **2**(5).

[9] Sutton, R. J.; Filip, M. R.; Haghighirad, A. A.; Sakai, N.; Wenger, B.; Giustino, F. and Snaith, H. J., August , (2018), **3**(8), 1787–1794.

[10] Wang, K.; Jin, Z.; Liang, L.; Bian, H.; Bai, D.; Wang, H.; Zhang, J.; Wang, Q. and Liu, S., December , (2018), **9**(1).

[11] Sanehira, E. M.; Marshall, A. R.; Christians, J. A.; Harvey, S. P.; Ciesielski, P. N.; Wheeler, L. M.; Schulz, P.; Lin, L. Y.; Beard, M. C. and Luther, J. M., October , (2017), **3**(10), eaao4204.

[12] Sanchez, S.; Christoph, N.; Grobety, B.; Phung, N.; Steiner, U.; Saliba, M. and Abate, A., October , (2018), **8**(30), 1802060.

[13] Becker, P.; Márquez, J. A.; Just, J.; Al-Ashouri, A.; Hages, C.; Hempel, H.; Jošt, M.; Albrecht, S.; Frahm, R. and Unold, T., April , (2019), page 1900555.

[14] Eperon, G. E.; Paternò, G. M.; Sutton, R. J.; Zampetti, A.; Haghighirad, A. A.; Cacialli, F. and Snaith, H. J., *Journal of Materials Chemistry A*, 2015, **3**(39), 19688–19695.

[15] Kulbak, M.; Gupta, S.; Kedem, N.; Levine, I.; Bendikov, T.; Hodes, G. and Cahen, D., January , (2016), **7**(1), 167–172.

[16] Murtaza, G. and Ahmad, I., September , (2011), **406**(17), 3222–3229.

[17] Brgoch, J.; Lehner, A. J.; Chabinyc, M. and Seshadri, R., December , (2014), **118**(48), 27721–27727.

[18] Jong, U.-G.; Yu, C.-J.; Kim, Y.-S.; Kye, Y.-H. and Kim, C.-H., September , (2018), **98**(12).

[19] Hendon, C. H.; Yang, R. X.; Burton, L. A. and Walsh, A., *Journal of Materials Chemistry A*, 2015, **3**(17), 9067–9070.

[20] Zhang, T.; Dar, M. I.; Li, G.; Xu, F.; Guo, N.; Grätzel, M. and Zhao, Y., *SCIENCE ADVANCES*, 2017, page 7.

[21] Roknuzzaman, M.; Ostrikov, K.; Wang, H.; Du, A. and Tesfamichael, T., October , (2017), **7**(1).

[22] Glazer, A. M., November , (1972), **28**(11), 3384–3392.

[23] Clark, S. J.; Segall, M. D.; Pickard, C. J.; Hasnip, P. J.; Probert, M. I. J.; Refson, K. and Payne, M. C., January , (2005), **220**(5/6).

[24] Segall, M. D.; Lindan, P. J. D.; Probert, M. J.; Pickard, C. J.; Hasnip, P. J.; Clark, S. J. and Payne, M. C., March , (2002), **14**(11), 2717–2744.

[25] Hamann, D. R.; Schlüter, M. and Chiang, C., November , (1979), **43**(20), 1494–1497.

[26] Ceperley, D. M. and Alder, B. J., August , (1980), **45**(7), 566–569.

[27] Perdew, J. P.; Burke, K. and Ernzerhof, M., October , (1996), **77**(18), 3865–3868.

[28] Perdew, J. P.; Ruzsinszky, A.; Csonka, G. I.; Vydrov, O. A.; Scuseria, G. E.; Constantin, L. A.; Zhou, X. and Burke, K., April , (2008), **100**(13), 136406.

[29] Pfrommer, B. G.; Côté, M.; Louie, S. G. and Cohen, M. L., February , (1997), **131**(1), 233–240.

[30] Heyd, J.; Scuseria, G. E. and Ernzerhof, M., June , (2006), **124**(21), 219906.

[31] Villars, P. and Cenzual, K., CsPbI3 high temperature (CsPbI3 ht1, T = 634 K) Crystal Structure: Datasheet from "PAULING FILE Multinaries Edition – 2012" in SpringerMaterials (https://materials.springer.com/isp/crystallographic/docs/sd_1627096).

[32] Even, J.; Pedesseau, L.; Jancu, J.-M. and Katan, C., September , (2013), **4**(17), 2999–3005.

[33] Kepenekian, M. and Even, J., July , (2017), **8**(14), 3362–3370.

[34] Leveillee, J.; Katan, C.; Zhou, L.; Mohite, A. D.; Even, J.; Tretiak, S.; Schleife, A. and Neukirch, A. J., October , (2018), **2**(10).

[35] Pedesseau, L.; Sapori, D.; Traore, B.; Robles, R.; Fang, H.-H.; Loi, M. A.; Tsai, H.; Nie, W.; Blancon, J.-C.; Neukirch, A.; Tretiak, S.; Mohite, A. D.; Katan, C.; Even, J. and Kepenekian, M., November , (2016), **10**(11), 9776–9786.

[36] Umari, P.; Mosconi, E. and De Angelis, F., May , (2015), **4**(1).

[37] Yang, Z.; Surrente, A.; Galkowski, K.; Miyata, A.; Portugall, O.; Sutton, R. J.; Haghighirad, A.; Snaith, H. J.; Maude, D. K.; Plochocka, P. and Nicholas, R. J., *ACS Energy Letters*, page 23.

[38] Rodina, A. V.; Dietrich, M.; Göldner, A.; Eckey, L.; Hoffmann, A.; Efros, A. L.; Rosen, M. and Meyer, B. K., August , (2001), **64**(11), 115204.

4

Mixed Halide Perovskite $\gamma-CsPbI_{3-x}Br_x$

Recently, it has been suggested that partial or total substitution of Iodine atoms by bromine atoms could stabilize the preferred perovskite black phase at low temperature [1–3]. Hence, it is necessary to investigate the electronic and optical characteristics of these materials. In this chapter, the structural, electronic, some carrier transport and optical properties of the all-inorganic cesium lead mixed halide perovskites $CsPbI_{3-x}Br_x$ with a low symmetry orthorhombic structure are systemically investigated. This chapter is a reproduced version of our paper [4] entitled "Insights on the opto-electronic structure of the inorganic mixed halide perovskites γ- $CsPbI_{3-x}Br_x$ with low symmetry black phase" published in the Journal of Alloys and Compounds.

4.1 Introduction

In the previous chapter in order to improve material stability, we have replaced the organic molecule FA and MA by smaller inorganic cation such Cs that stabilize their perovskite structure. The PCE of such compounds increases from 2.9% to 17.1% with better thermal stability [1–3, 5–13] . Indeed, most of the researchers paid less attention to the all-inorganic perovskites compared to the organic perovskites, due to the difficulty in their synthesis methods, however, recently all-inorganic perovskites were fabricated and exhibited good thermal stability. This fully inorganic compound has 1.72eV energy gap which is suitable for perovskite-Si tandem solar cells. In order to obtain the perovskite phase, thin films should be heated above 320° C, this high temperature damage the flexible substrates. Recently, it has been suggested that partial or total substitution of iodide by bromide $CsPbI_{3-x}Br_x$ could stabilize the preferred perovskite black phase at lower formation temperature [1–3]. Hence, it is necessary to investigate the electronic and optical characteristics of these compounds. In this chapter, the structural, electronic and optical properties including lattice parameter, cohesive energy, formation enthalpy, band structures, optical absorption spectra, effective masses, carrier mobility and band offset of the all-inorganic cesium lead mixed halide perovskite γ $CsPbI_{3-x}Br_x$ are systemically investigated by density functional theory. Indeed, we discuss the modelling and calculations of the inorganic mixed halide perovskites γ-$CsPbI_{3-x}Br_x$ for various Bromine concentrations. We have examined the structural and energy stability in the low symmetry black phase of γ-$CsPbI_{3-x}Br_x$. Our obtained results are compared and discussed with the available data.

4.2 Computational details

The calculations were carried out using the pseudo potential plane-wave (PP-PW) method as implemented in CASTEP [14, 15] code with the same parameter of previous chapter. Furthermore, to obtain the different concentration, in the first step we break the symmetry and substitute I by Br with an interval of 2Br atoms per conventional cell. We choose in our calculations the most energetically preferable position. In general, the best configuration

for fast convergence is the high symmetry ones.

4.3 Structure and materials stability

The unit cell of perovskite $CsPbI_3$ possess twelve I atoms Figure 4.1.We first determined the optimized lattice constants of both $CsPbI_3$ and $CsPbBr_3$ compounds and their solid solution $CsPbI_{3-x}Br_x$ by increasing the x from 0 to 1 with an interval of 0.167(2Br atoms).

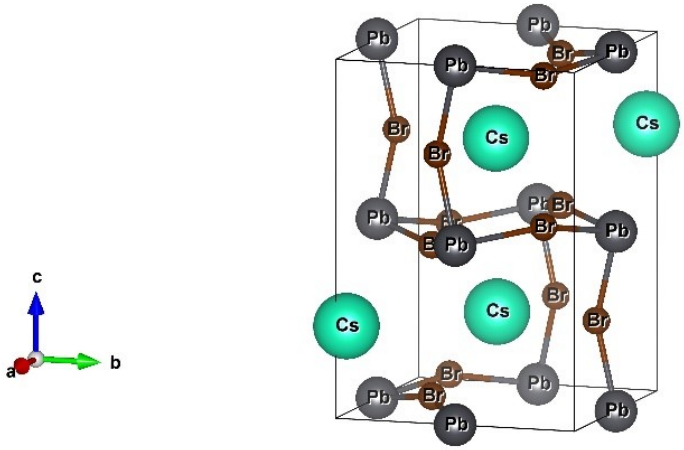

Figure 4.1: Crystal cell of $CsPbX_3$ perovskite used for different concentrations.

The detailed information about the calculated ground state parameters, such as, cell volume, cohesive energies, and formation energies of $CsPb(I_{1-x}Br_x)_3$ perovskites are given in Table 4.1 along with the available experimental and previously calculated values. In order to compute the formation energy we use Cs, Pb bulk $E_{Cs}^{Bulk} = -548.41, E_{Pb}^{Bulk} = -1657.94$ and Br_2, I_2 molecules $E_I^{mol} = -311.86$, and isolated Cs, Pb, I and Br atoms $E_{Cs}^{iso} = -547.4464, E_{Pb}^{iso} = -1653.8379, E, E_{Br}^{iso} = -362.7713, E_I^{iso} = -310.4721$ for the cohesive energy.

The magnitude of cohesive energy increase, while the equilibrium volume decrease. In Figure 4.2, we show cell volume vs Bromine concentration x. It is clear, the V vs x relation follows Veggar's law with a linear function $V = 948.8 - 155.4x$.

From (Table.4.1 and Figure 4.2), it is observed that, lattice volume values decreases with increasing x , this behavior is explained by the larger ionic radius of iodine compared

Table 4.1: Summary of equilibrium volume calculated using PBE and PBEsol beside cohesive and formation energies calculated through PBEsol method for $CsPbI_{3-x}Br_x$ perovskites compared to available experimental data.

Bromine contents x		0	0.17	0.33	0.5	0.67	0.83	1
Equilibrium volume	PBEsol	948.88	921.97	895.90	873.27	846.52	818.46	792.97
	exp	947 [9]						796.7 [16]
	PBE	983.5	979.0	948.4	931.6	898.2	870.8	839.2
Cohesive energy		-15.1	-15.37	-15.66	-15.90	-16.2	-16.52	-16.83
Formation energy		-5.94	-6.09	-6.26	-6.39	-6.57	-6.77	-6.97

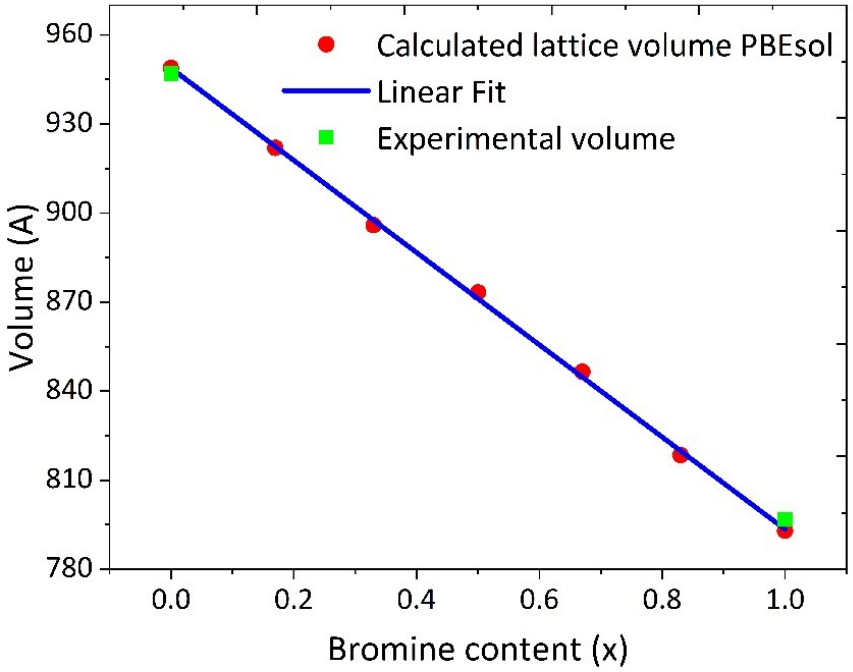

Figure 4.2: Lattice volume as a linear function of Br content x

to bromine. Our results are in good agreement with experimental values reported in [9] for $CsPbI_3(CsPbBr_3)$ compounds with disagreement of the order of 0.19%(0.47%). Moreover, the calculated negative cohesive and formation energies indicate the structural stability of these compounds.

We have already discussed the material stability using the cohesive, and formation energies through isolated and pure atom and molecules, but cannot give a direct estimation of material stability. Therefore, we calculate the formation enthalpies using the following chemical reaction: $CsX + PbX_2 = CsPbX_3$

The formation enthalpy can be calculated as follows:

$$\Delta Hf \approx \Delta Ef = E\left[CsPbX_3\right] - E\left[CsX\right] - E\left[PbX_2\right] \tag{4.1}$$

Our calculated formation enthalpies are presented in Figure 4.3. As we can see, all compounds have negative formation enthalpies and show an increase of their magnitudes as a function of Br content. This is a proof of thermodynamic stability of the present perovskites by the Br content increase.

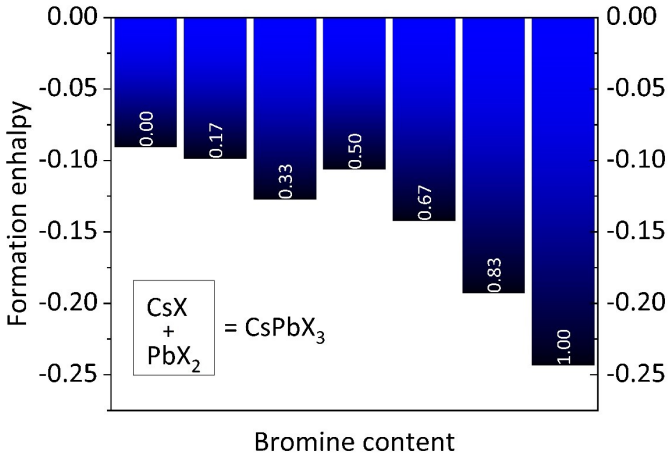

Figure 4.3: Calculated formation enthalpy of $CsPbI_{3-x}Br_x$ using PBEsol functional.

4.4 Electronic properties

In this section, we present the electronic band structures and deduce their effective masses at Γ point. The results of our calculations are presented in Figure 4.4. In general, the band structure of the seven configurations are quite similar, with gradual increase of band gaps. Moreover, all the studied compounds exhibit a direct band gap, where the conduction band minimum (CBM) and valence band maximum (VBM) are located at the Γ point. These semiconductors, by absorption of the photons, can generate an electron-hole pair (exciton) without any energy loss by interacting with phonons. In (Figure 4.5), we present the calculated band gaps while increasing the Br content x. The energy gap observed in $CsPbI_3$ is 1.75eV. It observed that when Br replaces two iodine atoms, the energy gap value increased to 1.81eV. When other iodine atoms are replaced, the band gap increases further. When all the 12 iodine atoms are replaced by of bromine atoms the energy gap reaches 2.16 eV. This is due to the higher electronegativity of bromine compared to iodine. Indeed, the change

of band gaps increases quadratically as Eg=0.2x2+0.22x+1.75 (Eg=0.11x2+0.38x+0.68) from 1.75 to 2.16(0.68 to 0.95) without (with) SOC respectively.

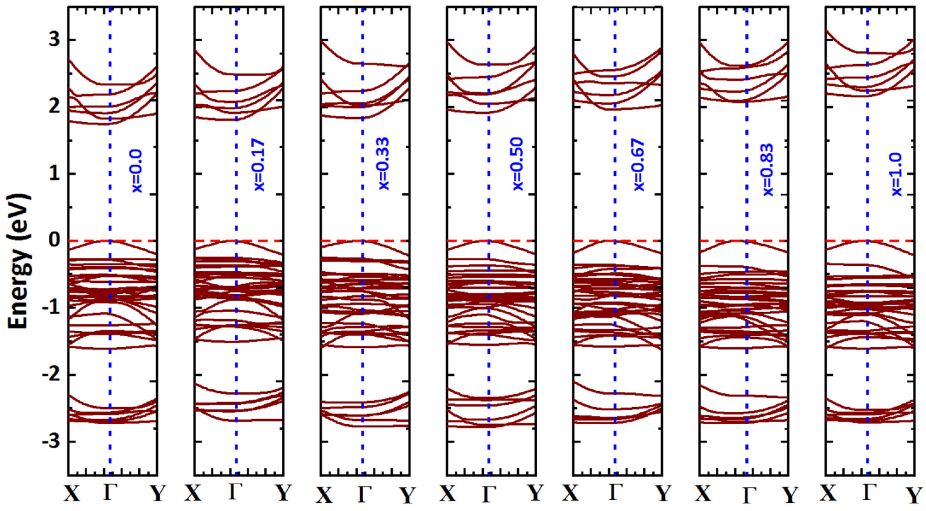

Figure 4.4: Calculated electronic band structures of mixed halide perovskites $CsPbI_{3-x}Br_x$ as a function of Br content x around the Γ point

The band edges have almost the same shape for all concentrations which indicate that all compounds have the same effective masse. The calculated band gaps without including SOC are found to be in good agreement with the experimental data such 1.73eV [13], 2.32eV [17] for $CsPbI_3$ and $CsPbBr_3$ respectively. This is due to the fortuitous error cancellation between overestimation from ignoring the SOC effect and the well-known DFT underestimation error as discussed in the previous chapter.

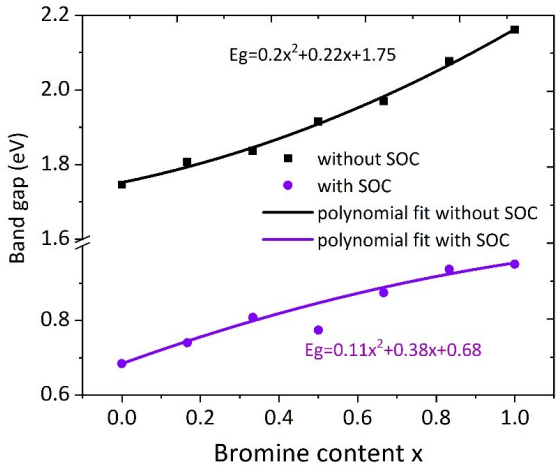

Figure 4.5: Band gaps as a function of Br content x.

4.5 Effective mass

In order to attain a deeper understanding of the charge carrier properties, we calculated the effective masses of electron and hole around the CBM and VBM at the Γ point using the parabolic approximation (see Eq 2.4) with refined energy band structure ($0.001 Å^{-1}$) separation between consecutive k-points. As discussed previously, lead-bromine substitution does not have high effect on the effective mass. Therefore, we present the calculated results of pure $CsPbI_3$($CsPbBr_3$) perovskites which exhibit very low effective masses 0.20(0.22) and 0.17(0.21) for hole and electron respectively. These values are comparable with other related compounds such $MAPbI_3$($MAPbBr_3$) m_h 0.19(0.23) m_e 0.18(0.21) [18]

4.6 Carrier mobility

The carrier mobility was calculated for pure compounds because of the similarity in the band dispersion. Deformation potential theory is used as explained in chapter 2 Using the previously mentioned relation (Eq 2.6) After the computation of effective mass, a small deformation (-3,3) along C axe was made. First, for the elastic parameter, Cii is directly used for both $CsPbI_3$ and $CsPbBr_3$ compounds. Using the distorted structures and from the energy band edge, the deformation potential constant was computed. In Table 4.2 Elastic constants, effective masses, deformation potentials and carrier mobilities of electrons and hole for both $CsPbI_3$ and $CsPbBr_3$ phase pure compounds were collected.

Table 4.2: Calculated effective masses, elastic constants, deformation potential constants,and carrier mobilities for $CsPbI_3$ and $CsPbBr_3$ perovskites. Masses are given in units of the free electron mass m_0.

Compounds	Carrier	Effective mass	Cii (GPa)	E (eV)	μ (cm2/V s)
$CsPbI_3$	E	0.17	26.9	18	409.15
	H	0.20		16	361.61
$CsPbBr_3$	E	0.21	39.18	23	225.70
	H	0.22		21	236.49

It is clear that all calculated mobility for both carrier are high, this is consistent with other previously reported results [19]. High electron and hole mobility are due to the very small effective masses.

4.7 Optical properties

In order to estimate the optical properties such as the photo-absorption coefficient, we first determined the frequency-dependent dielectric functions $\varepsilon = \varepsilon_1 + i\varepsilon_2$. The computed dielectric function are plotted in the range of 0-20 eV (Figure 4.6).

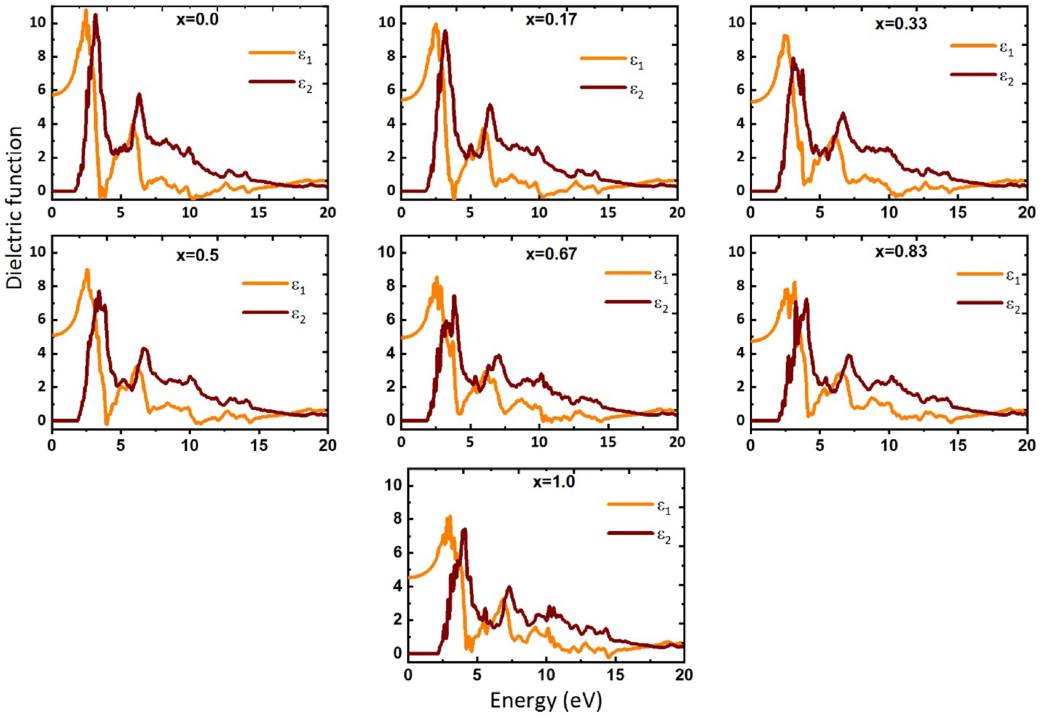

Figure 4.6: Calculated frequency dependent dielectric function for $CsPb(I_{1-x}Br_x)_3$ perovskites.

In the imaginary part, several main peaks are observed which originate from the electronic transitions from I-p/Br-p, Pb-s in the valence band to the Pb-p state in the conduction band. The static dielectric constants give information about the material electronic polarizability which decrease linearly with a function of Br content x as $\varepsilon_s(x) = 5.70 - 1.15x$ (see Figure 4.7).

The photo-absorption coefficient is a crucial factor for determining the light-harvesting ability of material as solar energy absorber . We have calculated this physical parameter using the dielectric functions through the relation (Eq 3.8). The calculated absorption coefficients of $CsPb(I_{1-x}Br_x)_3$ as function of photon energy are presented in Figure 4.8.

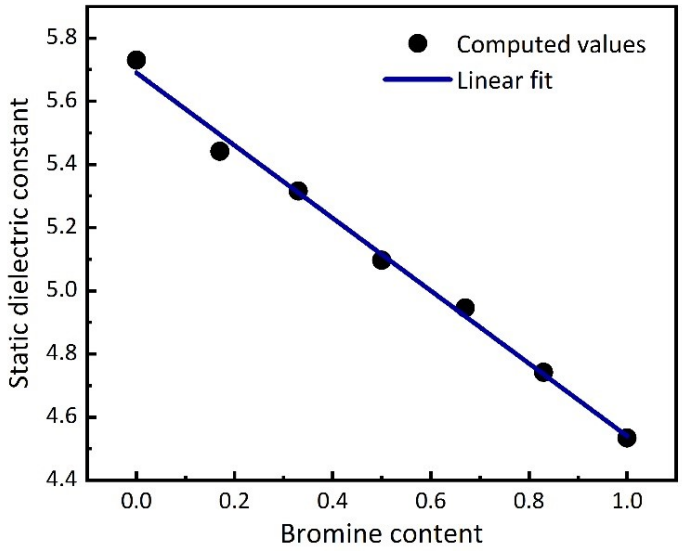

Figure 4.7: Static dielectric constants of mixed halide perovskites $CsPb(I_{1-x}Br_x)_3$ when increasing.

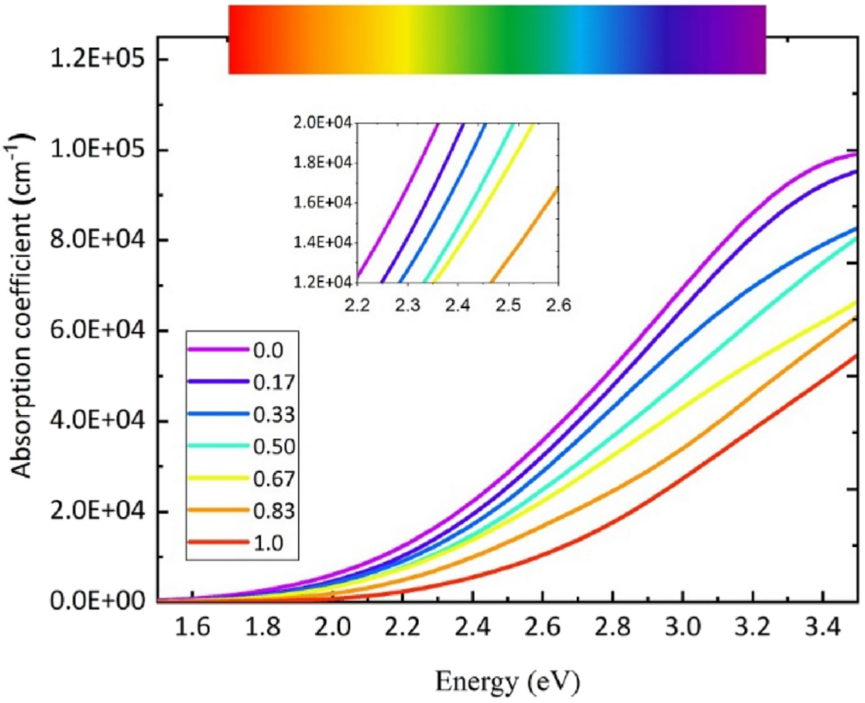

Figure 4.8: Calculated photo absorption coefficients for $CsPb(I_{1-x}Br_x)_3$ perovskites.

Obviously going from Iodine to bromine substitution decrease the absorption coefficient of mixed halide perovskite. In general, all these compounds are characterized by high absorption coefficient compared to other conventional materials such as CdTe as shown in

Figure 3.6.

4.8 Band alignment

The above result show that studied compounds have great potential to be powerful absorber materials. However, we should first compute their band position in order to choose the best suitable partner layers, which is very important for the solar device optimization. First, ionisation potential (IP) was computed using vacuum slab as we explained in chapter 2. For this purpose, 17 alternative layers were constructed. We choose 30 Å as empty space. The electrostatic potential as well as electronic density in the vacuum region were checked. It is clear there are no interaction between alternative layers. Energy difference was computed between vacuum level and one Cesium core state far away from surface and align VBM from bulk calculation using relation Eq 2.10. In the next figure, we compare IP to other partner to choose possible potential contact layers. Ionization potentials and band gaps of ETM and HTM have been taken from the literature [20].

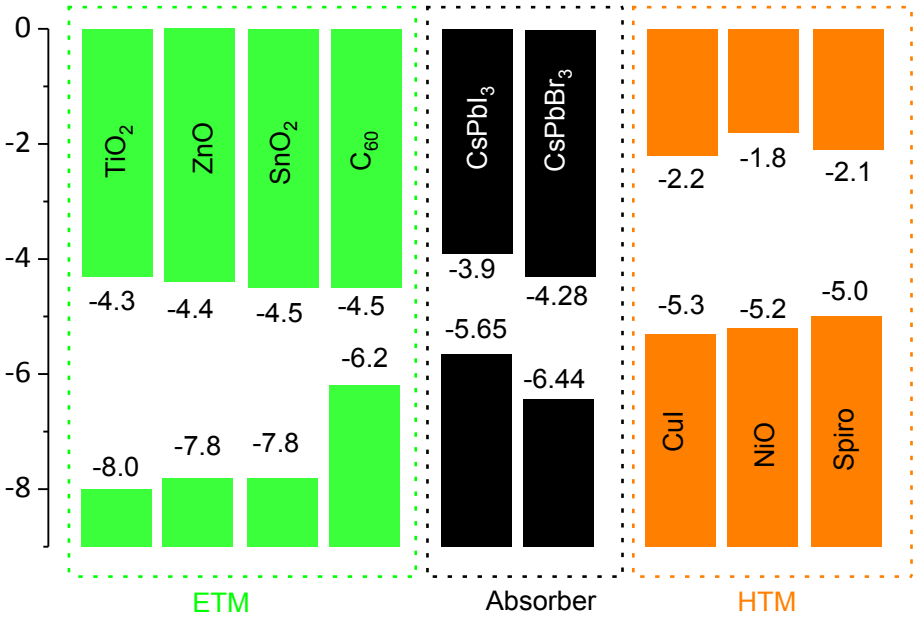

Figure 4.9: Band alignment of $CsPbBr_3$ and $CsPbI_3$. Ionization potentials and band gaps of other materials have been taken from the literature.

It is clear from Figure 4.9, that band alignments between both $CsPbI_3$ and $CsPbBr_3$ and the commonly used ETM show that all C_{60} SnO_2 ZnO and TiO_2 have lower CBM. There-

fore, these ETM are suitable for both $CsPbI_3$ and $CsPbBr_3$ based photovoltaic devices. The same note, for HTM all three compounds have higher VBM demonstrating that these HTM are also match well with both studied materials.

4.9 Conclusion

In summary, based on density functional pseudo-potential plane wave calculations, we have studied the material stability of seven $\gamma - CsPb(I_{1-x}Br_x)_3$ alloys perovskites. The electronic properties and light absorption characteristics of these compounds have been presented. The results show that, the iodine partial substitution significantly enhances material stability. Furthermore, the increase of Br content leads to a linear decrease of lattice volume. On the other hand, static dielectric constants decrease quadratically while the band gap increase quadratically with Br concentration x. After band alignments between both $CsPbI_3$ and $CsPbBr_3$ and the commonly used ETM and HTM it is clear that all studied material are suitable for both $CsPbI_3$ and $CsPbBr_3$ based photovoltaic devices.

Refrences

[1] Sanchez, S.; Christoph, N.; Grobety, B.; Phung, N.; Steiner, U.; Saliba, M. and Abate, A., October , (2018), **8**(30), 1802060.

[2] Ouedraogo, N. A. N.; Chen, Y.; Xiao, Y. Y.; Meng, Q.; Han, C. B.; Yan, H. and Zhang, Y., November , (2019), page 104249.

[3] Chen, M.; Ju, M.-G.; Garces, H. F.; Carl, A. D.; Ono, L. K.; Hawash, Z.; Zhang, Y.; Shen, T.; Qi, Y.; Grimm, R. L.; Pacifici, D.; Zeng, X. C.; Zhou, Y. and Padture, N. P., December , (2019), **10**(1).

[4] Fadla, M. A.; Bentria, B.; Benghia, A.; Dahame, T. and Goumri-Said, S., August , (2020), **832**, 154847.

[5] Kojima, A.; Teshima, K.; Shirai, Y. and Miyasaka, T., May , (2009), **131**(17), 6050–6051.

[6] Lee, M. M.; Teuscher, J.; Miyasaka, T.; Murakami, T. N. and Snaith, H. J., November , (2012), **338**(6107), 643–647.

[7] Snaith, H. J., November , (2013), **4**(21), 3623–3630.

[8] Katan, C.; Mercier, N. and Even, J., March , (2019), **119**(5), 3140–3192.

[9] Sutton, R. J.; Filip, M. R.; Haghighirad, A. A.; Sakai, N.; Wenger, B.; Giustino, F. and Snaith, H. J., August , (2018), **3**(8), 1787–1794.

[10] Wang, Z.; Ganose, A.; Niu, C. and Scanlon, D. O., *Journal of Materials Chemistry A*, 2018, **6**(14), 5652–5660.

[11] Sanehira, E. M.; Marshall, A. R.; Christians, J. A.; Harvey, S. P.; Ciesielski, P. N.; Wheeler, L. M.; Schulz, P.; Lin, L. Y.; Beard, M. C. and Luther, J. M., October , (2017), **3**(10), eaao4204.

[12] Becker, P.; Márquez, J. A.; Just, J.; Al-Ashouri, A.; Hages, C.; Hempel, H.; Jošt, M.; Albrecht, S.; Frahm, R. and Unold, T., April , (2019), page 1900555.

[13] Eperon, G. E.; Paternò, G. M.; Sutton, R. J.; Zampetti, A.; Haghighirad, A. A.; Cacialli, F. and Snaith, H. J., *Journal of Materials Chemistry A*, 2015, **3**(39), 19688–19695.

[14] Segall, M. D.; Lindan, P. J. D.; Probert, M. J.; Pickard, C. J.; Hasnip, P. J.; Clark, S. J. and Payne, M. C., March , (2002), **14**(11), 2717–2744.

[15] Clark, S. J.; Segall, M. D.; Pickard, C. J.; Hasnip, P. J.; Probert, M. I. J.; Refson, K. and Payne, M. C., January , (2005), **220**(5/6).

[16] Villars, P. and Cenzual, K., rt-CsPbBr3 (CsPbBr3 rt) Crystal Structure: Datasheet from "PAULING FILE Multinaries Edition – 2012" in SpringerMaterials (https://materials.springer.com/isp/crystallographic/docs/sd_1623827).

[17] Liu, X.; Tan, X.; Liu, Z.; Ye, H.; Sun, B.; Shi, T.; Tang, Z. and Liao, G., February , (2019), **56**, 184–195.

[18] Jong, U.-G.; Yu, C.-J.; Ri, J.-S.; Kim, N.-H. and Ri, G.-C., September , (2016),

94(12), 125139.

[19] Kang, Y. and Han, S., October , (2018), **10**(4), 044013.

[20] Yang, Z.; Dou, J. and Wang, M., *Solar RRL*, 2018, **2**(12), 1800177.

5

Defect Chemistry of $CsPbI_3$ and $CsPbBr_3$ Perovskite

Full inorganic perovskite are one of the most promising photovoltaic material due to their exceptional optoelectronic properties, which are extensively discussed in the previous chapters. The high PCE is directly related to their low recombination rate even in the presence of defect. In this chapter, we try to give in depth understanding of defect chemistry of $CsPbI_3$ and $CsPbBr_3$ perovskite through DFT method.

5.1 Introduction

Hybrid organic inorganic halide perovskite are promising materials for high efficient and low cost solar cells. This is due to their optimal optoelectronic properties such as suitable and tunable band gap, high optical absorption coefficient, high electron and hole mobility, low exciton binding energy, large diffusion length and high life time. Beside their surprising defect tolerance, which is one of most required characteristic for an efficient photovoltaic device i.e. the intrinsic defect will not destroy the performance of solar cells by trapping the generated carriers. However, the semiconductor should be elaborated in special condition in order to reduce the Shockley-Read-Hall recombination rate, as consequent the generated carriers lives enough time to be extracted and thus a high Voc.

Many recent works show that hybrid halide perovskite which are prepared by a cheap solution processing at low temperature have a low density of traps of 10^{11} cm^{-3} and 10^{16} cm^{-3} for single crystal [1, 2] and polycrystalline [1, 3, 4] material respectively. Other report, using hybrid DFT calculation shown that iodine interstitial could induce a deep levels in $MAPbI_3$ gap. Moreover, Daniele Meggiolaro and co-worker [5], by combining first-principles calculations with photoluminescence and transient absorption measurements, showed that iodine chemistry could determines the defect tolerance in $MAPbI_3$ perovskite and explain the enhancement of the optoelectronic properties by doping. they also demostrated that chlorine and bromine doping could deactivate iodine hole traps by shifting the transition levels from deep to shallow. However, compared to HOIP that was studied extensively, a light study on full inorganic perovskite was carried out. Indeed, among the purely inorganic halide perovskite, defect properties of $CsPbBr_3$ has been studied by Ref [6] using DFT calculation. Like their cousin (MAPbI3) this compound show a high defect tolerance, with most of defects introducing shallow traps in the energy gap and few defects create deep transition levels with high formation energy.

The aims of this chapter is to give an in-depth understanding of the formation mechanisms of intrinsic point defect in full inorganic perovskite and discuss their effect on PSCs efficiency through DFT method.

5.2 Computational details

First-principles pseudo potential plane wave calculations was carried out using Quantum espresso code [7]. Norm conserving pseudopotential[8–10] was used. Plane-wave cut-off energy of 50 Ry and 4 × 3 × 4 k-point with an energy convergence threshold of 10^{-7} eV per unit cell. Calculations were carried out using PBEsol-GGA exchange correlation potential. [11]. In order to simulate point defect, 80 atoms supercells were used 221(212) for $CsPbI_3$ ($CsPbBr_3$). The defect formation energy was calculated including potential alignment and electrostatic corrections using the relation Eq 2.13. In this work, we use FNV [12] correction scheme and [13] to include dielectric constant anisotropy.

5.3 Pristine structure

We first perform our study on the pristine structure of $CsPbI_3$ and $CsPbBr_3$ perovskites in their orthorhombic phase (see Figure 5.1) which is the most stable perovskite structure.

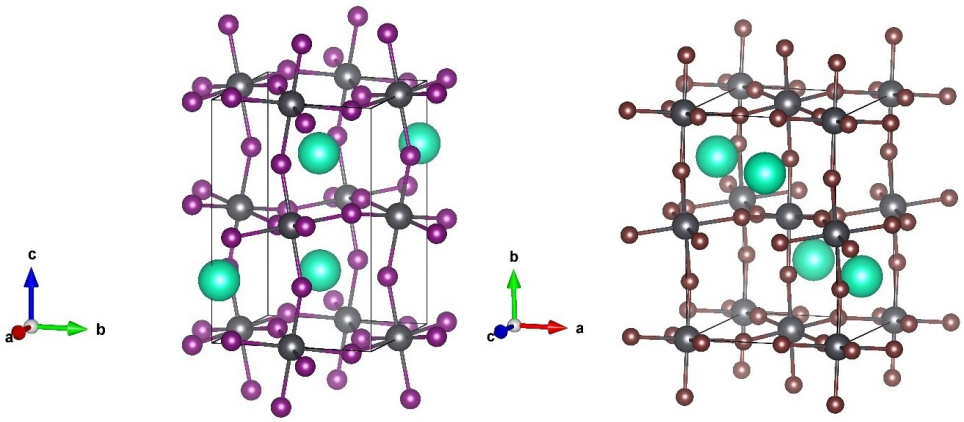

Figure 5.1: Crystal structure of $CsPbI_3$ and $CsPbBr_3$ perovskite. The green, gray, purple and brown balls represent Cs, Pb, I and Br atoms respectively.

In Table 5.1, we summarize the calculated lattice parameters, formation energies and heat of formation for the two compounds compared with other previously published experimental data.

It is clear that our calculated lattice parameters show a good agreement with the experimental values. Indeed, it is common knowledge that PBEsol-GGA gives more accurately values compared to PBE-GGA and LDA. Moreover, $CsPbBr_3$ show much better stability

Table 5.1: Calculated ground state properties: lattice parameter, Heat formation (from CsI CsBr $PbBr_2$ and PbI_2 precursor), and formation energy (from Cs Pb bulk and Br_2 I_2 molecules) for $CsPbI_3$ and $CsPbBr_3$ perovskite using PBEsol.

	Lattice parameter (Å)	Heat of formation(eV)	Formation energy(eV)
$CsPbBr_3$	8.37, 11.63, 7.99	-0.29	-8.01
	8.37, 11.49, 7.61 [14]		
	8.25, 11.75, 8.20 [15]		
$CsPbI_3$	8.91, 8.34, 12.32	-0.08	-6.89
	8.86, 8.58, 12.47 [16]		

than $CsPbI_3$, which already discussed in the previous chapters.

5.4 Defective $CsPbBr_3$

5.4.1 Chemical potential

In order to simulate point defect for different growth conditions of $CsPbBr_3$ we compute chemical potential limits using CsBr, $PbBr_2$, Cs, Pb bulks and Br_2 molecule. $CsPbBr_3$ is formed when the following chemical potential condition is satisfied:

$$\mu_{Cs} + \mu_{P_b} + 3\mu_{Br} = \Delta H \, (-8.01 \text{ for } CsPbBr_3) \tag{5.1}$$

To avoid the formation of CsBr and $PbBr_2$ secondary phases we must have the following limits:

$$\mu_{Cs} + \mu_{Br} < \Delta H_{CsBr} = -3.81eV$$

$$\mu_{Pb} + 2\mu_{Br} < \Delta H_{PbBr_2} = -3.91eV$$

Now we can plot the thermodynamic stability regions Figure 5.2.

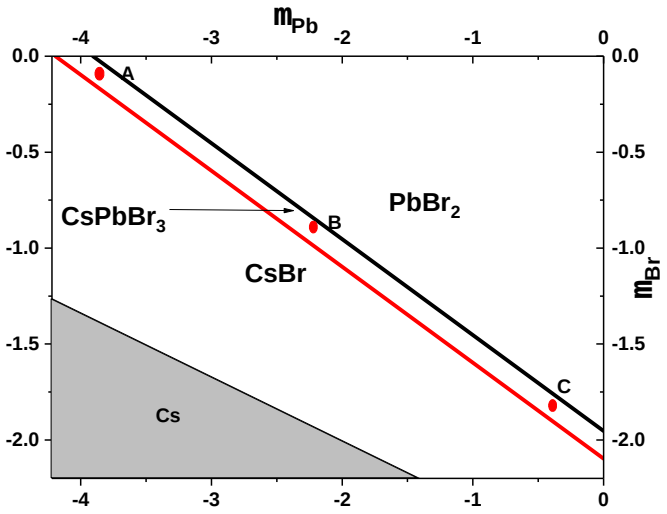

Figure 5.2: Stability diagram of γ-$CsPbBr_3$, CsBr and $PbBr_2$ compounds obtained by PBEsol calculations. A, B, and C points represent Pb-poor/Br rich (A), Pb/Br-medium (B), and Pb-rich/Br-poor (C) growth conditions.

It is clear that $CsPbBr_3$ compounds have low dissociation energy, therefore, the growth condition should carefully be controlled in order to form the exact stoichiometry. The observed long shape gives the opportunity to form n-type or p-type absorber during different growth condition.

5.4.2 Defect formation energy

The Defect formation energies (DFE) of charged defects are calculated using the Eq 2.13 for a supercell containing 80 atoms which is sufficient for this type of study. First, we perform structure relaxation until forces for each atom are below 0.003 Ry/au. All possible intrinsic point defects for $CsPbBr_3$ were studied, including three vacancies (V_{Cs}, V_{Pb}, and V_{Br}), six antisites (Cs_{Pb}, Cs_{Br}, Pb_{Cs}, Pb_{Br}, Br_{Cs} and Br_{Pb}) and three interstitials (i_{Cs}, i_{Pb}, i_{Br}). We chose three representative points, which are marked by red points (Figure 5.2) Pb-poor/Br rich (A), Pb/Br-medium (B), and Pb-rich/Br-poor (C) growth conditions. In Table 5.2, we present the calculated DFE for neutral state of $CsPbBr_3$ compound.

As presented in Table 5.2 Cesium vacancy is the dominant defect under Bromine rich condition, since it has the lowest formation energy of 0.049 eV. V_{Cs} also is dominant under Pb moderate condition with formation energy of 0.815 eV. In addition, under Br poor condition all defects have formation energies higher than that of Pb_{Cs} antisites of 1.197eV.

Table 5.2: Calculated defect formation energy of neutral defects for $CsPbBr_3$.

	V_{Cs}	V_{Pb}	V_{Br}	Cs_{Pb}	Cs_{Br}	Pb_{Cs}	Pb_{Br}	Br_{Cs}	Br_{Pb}	i_{Cs}	i_{Pb}	i_{Br}
A	0.049	0.199	3.081	0.530	6.869	2.937	7.398	0.801	0.615	3.393	5.413	0.321
B	0.815	1.839	2.279	1.404	5.301	2.063	4.956	2.369	3.057	2.627	3.773	1.123
C	1.785	3.659	1.349	2.254	3.401	1.213	2.206	4.269	5.807	1.657	1.953	2.053

V_{Br} also shows low formation energy compared to other defects under this condition. All these results show good agreement with previously reported results [6].

In order to investigate ionization energy we compute defect formation energies of different charge states including electrostatic correction as well as potential alignment (for more detail see chapter 2). Charged DFE for $CsPbBr_3$ compound in different growth condition are collected in the Figure 5.3.

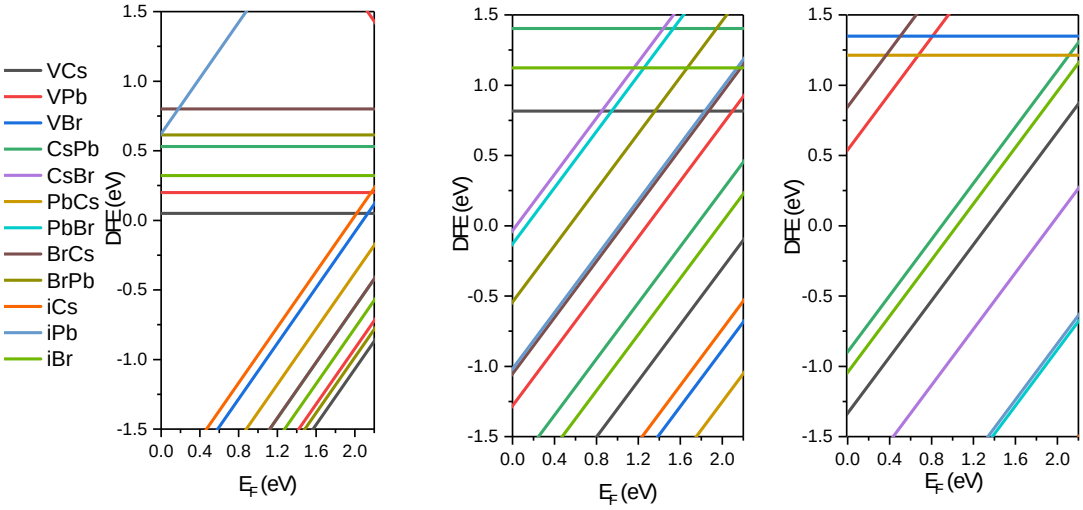

Figure 5.3: The calculated formation energies of intrinsic point defects in $CsPbBr_3$ at A, B, and C growth conditions. We ignored defects with much high formation energies.

It is clear that only some defects have low formation energy (-1.5 1.5) and all defects don't create any deep level which explain the high performance of these compounds, namely large carrier life time and diffusion length as well as high V_{oc}. However, other works by mean of HSE06+SOC show that Bri and V_{Pb} crate deep levels. We should note that HSE06+SOC is very expensive method, therefor, they only perform HSE06+SOC energy calculation without relaxation (relaxation using PBE) that could not much affect the band gap value but we assume that it has significant effect on the calculated formation en-

ergies. Very small residual forces can have significant change on the computed energy and therefore may change the results and influence our understanding.

5.5 Defective $CsPbI_3$

5.5.1 Chemical potential

The same method is used for $CsPbI_3$, we first compute chemical potential limits using CsI, PbI_2, Cs, Pb bulks and I_2 molecule in order to compute point defect formation energy for different growth conditions. $CsPbI_3$ should be formed when the following chemical potential condition is satisfied:

$$\mu_{Cs} + \mu_{Pb} + 3\mu_I = \Delta H_{CsPbI_3}(-6.89) \tag{5.2}$$

To avoid the formation of CsI and PbI_2 secondary phases. We must apply the following limits:

$$\mu_{Cs} + \mu_I < \Delta H_{CsI} = -3.43eV$$

$$\mu_{Pb} + 2\mu_I < \Delta H_{PbI_2} = -3.38eV$$

Now we can plot the thermodynamic stability regions

As we can see in Figure 5.4, it is clear that $CsPbI_3$ compound have lower dissociation energy compared to $CsPbBr_3$, which agree well with the previously presented results . Of course, the growth conditions should carefully be controlled in order to form the exact stoichiometry. However, like $CsPbBr_3$ this long shape leads to a flexible conductivity from n-type, intrinsic to p-type absorber using different growth conditions.

5.5.2 Defect formation energy

The formation energies of charged defects are calculated using the same 80 atoms supercell size and conditions . All possible intrinsic point defects in $CsPbI_3$ were studied, including three vacancies (V_{Cs}, V_{Pb}, and V_I), six antisites (Cs_{Pb}, Cs_I, Pb_{Cs}, Pb_I, I_{Cs}, I_{Pb}) and

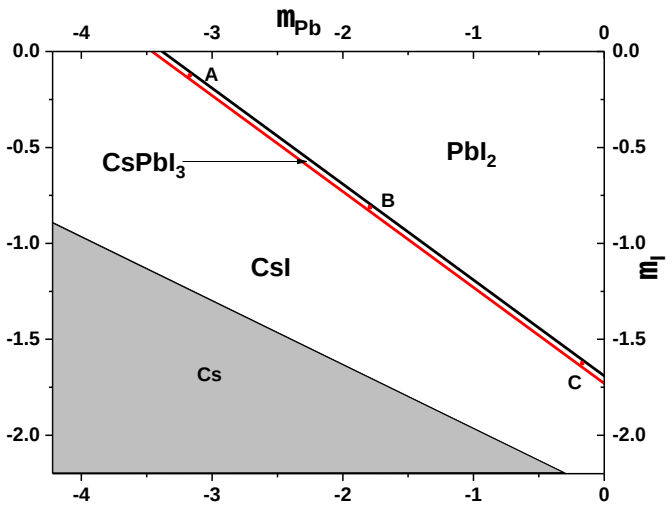

Figure 5.4: Stability diagram of γ-$CsPbI_3$, CsI and PbI_2 compounds obtained by PBEsol calculations. A, B, and C points represent Pb-poor/I rich (A), Pb/I-medium (B), and Pb-rich/I-poor (C) growth conditions.

three interstitials (i_{Cs}, i_{Pb}, i_I). We choose three representative points, which are marked by points (Figure 5.4) : Pb-poor/I rich (A), Pb/I-medium (B), and Pb-rich/I-poor (C) growth conditions. DFE for $CsPbI_3$ compound for neutrals state collected in the Table 5.3.

Table 5.3: Calculated defect formation energy of neutral defects for $CsPbI_3$.

	V_{Cs}	V_{Pb}	V_I	Cs_{Pb}	Cs_I	Pb_{Cs}	Pb_I	I_{Cs}	I_{Pb}	i_{Cs}	i_{Pb}	i_I
A	0.371	0.354	2.110	0.554	5.113	2.283	5.698	0.224	0.106	2.471	4.395	0.702
B	1.057	1.732	1.422	1.246	3.739	1.591	3.632	1.597	2.171	1.786	3.018	1.390
C	1.867	3.356	0.610	2.060	2.117	0.777	1.196	3.220	4.608	0.975	1.393	2.202

It is clear that many defects have a low formation energy under I rich condition, contrary to I medium and I poor conditions. Therefore to avoid this defect it is possible to change growth conditions to medium especially for V_{Pb} and i_I defects which could create colour centres according to other studies [5, 6].

In order to investigate the defect chemistry we compute the defect formation energy of different charge states. Charged DFE for $CsPbI_3$ compound in different growth condition are collected in the Figure 5.5.

It is clear that DFE have almost a similar behavior to $CsPbBr_3$, only several defects have low formation energies (-1.5 1.5). There are no deep levels only few ionization level were pinned inside CB, which explains the high performance of these compounds.

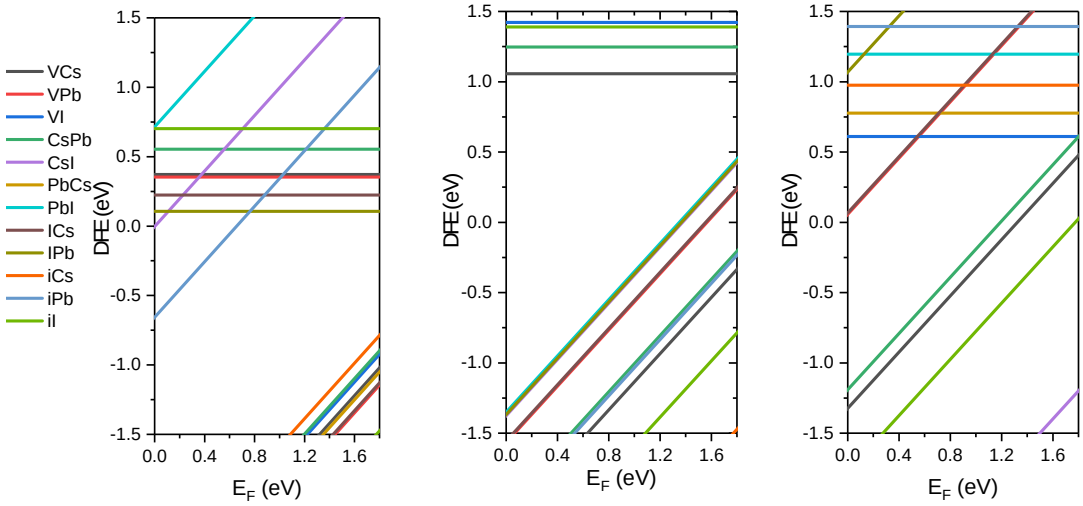

Figure 5.5: The calculated formation energies of intrinsic point defects in $CsPbI_3$ at A, B, and C growth condition. We ignore defects with much high formation energies.

5.6 Conclusion

We have performed DFT calculations to study the defect properties of $CsPbI_3$ $CsPbBr_3$ perovskite. Several defects can be easily formed under halide (Br,I) rich conditions especially for $CsPbI_3$ perovskite. Thus avoiding these growth conditions should be used to reduce the defect concentration. We did not find any deep levels unlike previously reported in [5, 6]. This result discrepancy may be explained by the used calculation method and parameters. However, we all agree that intrinsic defects that may create deep levels have high formation energies especially under specific growth conditions. We should note here that we have studied only pure orthorhombic phases which represents the most stable perovskite structure however other phases may be formed and create deep energy levels or low energy defect. Other trap states may be formed in the interface between perovskite layers and hole or electron transport material.

Refrences

[1] Chen, Y.; Yi, H. T.; Wu, X.; Haroldson, R.; Gartstein, Y. N.; Rodionov, Y. I.; Tikhonov, K. S.; Zakhidov, A.; Zhu, X.-Y. and Podzorov, V., August , (2016), **7**(1), 12253.

[2] Adinolfi, V.; Yuan, M.; Comin, R.; Thibau, E. S.; Shi, D.; Saidaminov, M. I.; Kanjanaboos, P.; Kopilovic, D.; Hoogland, S.; Lu, Z.-H.; Bakr, O. M. and Sargent, E. H., *Advanced Materials (Deerfield Beach, Fla.)*, 2016, **28**(17), 3406–3410.

[3] Leijtens, T.; Eperon, G. E.; Barker, A. J.; Grancini, G.; Zhang, W.; Ball, J. M.; Kandada, A. R. S.; Snaith, H. J. and Petrozza, A., November , (2016), **9**(11), 3472–3481.

[4] deQuilettes, D. W.; Vorpahl, S. M.; Stranks, S. D.; Nagaoka, H.; Eperon, G. E.; Ziffer, M. E.; Snaith, H. J. and Ginger, D. S., May , (2015), **348**(6235), 683–686.

[5] Meggiolaro, D.; Motti, S. G.; Mosconi, E.; Barker, A. J.; Ball, J.; Perini, C. A. R.; Deschler, F.; Petrozza, A. and Angelis, F. D., March , (2018), **11**(3), 702–713.

[6] Kang, J. and Wang, L.-W., January , (2017), **8**(2), 489–493.

[7] Giannozzi, P.; Baroni, S.; Bonini, N.; Calandra, M.; Car, R.; Cavazzoni, C.; Ceresoli, D.; Chiarotti, G. L.; Cococcioni, M.; Dabo, I.; Corso, A. D.; Gironcoli, S. d.; Fabris, S.; Fratesi, G.; Gebauer, R.; Gerstmann, U.; Gougoussis, C.; Kokalj, A.; Lazzeri, M.; Martin-Samos, L.; Marzari, N.; Mauri, F.; Mazzarello, R.; Paolini, S.; Pasquarello, A.; Paulatto, L.; Sbraccia, C.; Scandolo, S.; Sclauzero, G.; Seitsonen, A. P.; Smogunov, A.; Umari, P. and Wentzcovitch, R. M., September , (2009), **21**(39), 395502.

[8] Hamann, D. R., August , (2013), **88**(8), 085117.

[9] Hamann, D. R.; Schlüter, M. and Chiang, C., November , (1979), **43**(20), 1494–1497.

[10] van Setten, M.; Giantomassi, M.; Bousquet, E.; Verstraete, M.; Hamann, D.; Gonze, X. and Rignanese, G.-M., May , (2018), **226**, 39–54.

[11] Perdew, J. P.; Ruzsinszky, A.; Csonka, G. I.; Vydrov, O. A.; Scuseria, G. E.; Constantin, L. A.; Zhou, X. and Burke, K., April , (2008), **100**(13), 136406.

[12] Freysoldt, C.; Neugebauer, J. and Van de Walle, C. G., January , (2009), **102**(1), 016402.

[13] Kumagai, Y. and Oba, F., May , (2014), **89**(19), 195205.

[14] Tomanová, K.; Čuba, V.; Brik, M. G.; Mihóková, E.; Martinez Turtos, R.; Lecoq, P.; Auffray, E. and Nikl, M., January , (2019), **7**(1), 011104.

[15] Linaburg, M. R.; McClure, E. T.; Majher, J. D. and Woodward, P. M., April , (2017), **29**(8), 3507–3514.

[16] Sutton, R. J.; Filip, M. R.; Haghighirad, A. A.; Sakai, N.; Wenger, B.; Giustino, F. and Snaith, H. J., August , (2018), **3**(8), 1787–1794.

Conclusion

Conclusion

In this thesis, first-principles method has been used to study the emergent perovskite materials for optoelectronic applications, with a main focus on photovoltaic applications. Background information regarding photovoltaic as well as perovskite materials, which are considered in this thesis were provided in Chapter 1. The next chapter outlined the first-principles methods with focus on the theoretical methods used in this thesis to extract physical parametrers. We intend to exhibit how density functional theory was used for compute specific properties such as carrier mobility and defect properties.

In Chapter 3, Ab initio techniques were used to investigate the electronic structure of full inorganic Cesium Lead Iodide $CsPbI_3$ polymorphs. Total replacement of the organic molecule in hybrid organic-inorganic perovskite with Cs^+ cation was used to increase the chemical stability. The obtained results demonstrate that the lower symmetry orthorhombic Pnam phase is more energetically favourable compared to tetragonal phase and the high symmetric cubic phase. From density of state, it is clear that lead atom play significant role in the electronic and optical properties, which has much influence on light absorption of material. All studied polymorphs have low effective masses and high absorption coefficient.

In chapter 4, to increase material stability and tune band gap as well as other optoelectronic properties we use solid solution approach to study the low symmetry black $CsPb(I_{3-x}Br_x)$ perovskites. The electronic properties and light absorption characteristics of black phase has been presented, too. The iodine – bromine partial substitution significantly enhances material stability. Furthermore, static dielectric constants decrease quadratically while the band gap increase quadratically with a function of Br content this result can be used in order to obtain ideal concentration to tune band gap. Band alignment approach was used to find suitable electron and hole materials.

The main focus of the last chapter was to understand the high power conversion efficiency of perovskite materials which elaborated using simple solid solution process. In this chapter, by mean of super cell approach and using FNV-KO scheme we investigate the defect chemistry of $CsPbI_3$ and $CsPbBr_3$ perovskites. Indeed, all possible intrinsic point

defects in both $CsPbBr_3$ and $CsPbI_3$ were studied including formation energies and charge transition levels. It is clear that the most defect create shallow level without any deep level. The intrinsic defect that may create a deep level have high formation energies especially under specific growth condition (Br/I poor condition). We should mention, during this thesis only most stable and pure orthorhombic phase was studied. However, other phase may formed under specific conditions and create a deep level in lower energy, other trap state may formed in the interface between perovskite layers and hole or electron transport material.

Our future aim is to use more sophisticated techniques to obtain best possible results, study this kind of materials in large-scale level, and apply machine learning to get in-depth understanding on structure-property relationship and develop ML model to predict defect chemistry of PSCs.